



HAL
open science

In situ observation of crystal reorientation in polygranular graphite by synchrotron X-ray diffraction and neutron imaging

Thomas Zillhardt, Genoveva Burca, Wolfgang Ludwig, Dong Liu, T. James Marrow

► To cite this version:

Thomas Zillhardt, Genoveva Burca, Wolfgang Ludwig, Dong Liu, T. James Marrow. In situ observation of crystal reorientation in polygranular graphite by synchrotron X-ray diffraction and neutron imaging. *Carbon*, 2023, 214, pp.118378. 10.1016/j.carbon.2023.118378 . hal-04305325

HAL Id: hal-04305325

<https://hal.science/hal-04305325>

Submitted on 24 Nov 2023

HAL is a multi-disciplinary open access archive for the deposit and dissemination of scientific research documents, whether they are published or not. The documents may come from teaching and research institutions in France or abroad, or from public or private research centers.

L'archive ouverte pluridisciplinaire **HAL**, est destinée au dépôt et à la diffusion de documents scientifiques de niveau recherche, publiés ou non, émanant des établissements d'enseignement et de recherche français ou étrangers, des laboratoires publics ou privés.

In Situ Observation of Crystal Reorientation in Polygranular Graphite by Synchrotron X-Ray Diffraction and Neutron Imaging

Thomas Zillhardt^{1*}, Genoveva Burca^{2,6}, Wolfgang Ludwig^{4,5}, Dong Liu⁵, T. James Marrow¹

¹ Department of Materials, University of Oxford, Parks Road, Oxford, OX1 3PH Oxford, UK

² STFC, Rutherford Appleton Laboratory, Didcot OX11 0QX, UK

³ European Synchrotron Radiation Facility, 71 Avenue des Martyrs, 38000 Grenoble, France

⁴ MatéIS, INSA Lyon, France

⁵ HH Wills Physics Laboratory, Tyndall Avenue, Bristol, BS8 1TL, UK

⁶ Diamond Light Source Ltd, Didcot OX11 0DE, UK

Keywords: X-ray diffraction, crystal reorientation, nuclear graphite, Bragg-edge neutron imaging.

**** for submission to Carbon ****

Please use track changes

Abstract

The capacity of polygranular graphite to accommodate strain is important to its use within structural components of advanced nuclear fission reactors. This study has used in situ neutron and synchrotron X-ray experiments to demonstrate that reorientation of crystal domains accompanies the accommodation of strain in unirradiated Gilsocarbon (GCMB/IM24) graphite. Orientation changes were observed using 3D X-ray Diffraction, and local changes in neutron scattering were also observed with energy-resolved Bragg-edge neutron imaging. In both cases, this behaviour at the crystal level was partially recovered when the load was removed. This study provides new evidence for crystal deformation mechanisms that contribute to unirradiated polycrystalline graphite's non-linearity and the development of permanent set, and explain the effects of irradiation on graphite elastic behaviour.

1 Introduction

Polygranular graphite is an important functional and structural material in energy applications. For instance, large blocks of synthetic graphite have been used in the steel refining industry for Electric Arc Furnaces (EAF) for many years [1] and as electrodes in Electro-Spark Deposition (ESD) to improve corrosion resistance of metals [2]. Graphite is also widely used in the anodes of lithium-ion batteries, in which its *in operando* dimensional changes are important [3,4]. For over half a century, graphite has been critical as a neutron moderator in gas-cooled nuclear fission reactors [5] and novel graphite microstructures are now being investigated for use in next-generation advanced fission reactors [6], particularly thermal neutron versions of Very High Temperature (VHTR) [7,8] and Molten Salt Reactors (MSR) [9]. Graphite's thermal properties led to its consideration in fusion reactors as a potential plasma facing component [10], and it is also of interest for its tritium recycling capabilities [11].

The room temperature elastic properties of unirradiated polygranular graphite are non-linear [12]. Fine scale microcracks in the microstructure ('Mrozowski' accommodation pores [13]) have an important influence on its thermal expansion and elastic modulus, and it has been proposed that deformation mechanisms including microcracking decrease the elastic modulus with increasing tensile strain [13, 14]. In nuclear applications, significant dimensional and property changes occur with irradiation, which can lead to the development of internal stress and mechanical damage [5]. Irradiation also removes the non-linearity of polygranular graphite's elastic deformation [14] and affects its strength, stiffness and fracture behaviour [15].

Polygranular synthetic graphite microstructures are complex and depend on the manufacturing processes and raw materials [16]. This work considers Gilsocarbon

graphite (GCMB/IM1-24), which is used as moderator, reflector and fuel sleeves in the UK Advanced Gas-Cooled Reactors (AGR). The spherical Gilsonite filler particles, together with the vibration moulding manufacturing process, give it near-isotropic properties. Studies of graphite crystal properties are necessary to provide essential information for microstructure-based predictive models for the effects of irradiation and oxidation [17,18]. Such models are required to understand the general effects of irradiation and temperature on graphite properties and will support the design and operation of advanced fission reactors for which new isotropic graphites are being developed [19].

The crystals in synthetic graphite have Bernal ABAB stacking of hexagonal planes that can shear by basal dislocation glide [20] and kink band formation [21,22]. Twinning can also occur in graphite [23], [24], and has been defined as a rotation of approximately 20° about $\langle 1\bar{1}01 \rangle$ [25]. Twinning under load in natural graphite flakes has been observed [26] and it has also been reported in a micro-mechanical study of a neutron-irradiated synthetic graphite that twins recover once the load is removed [27]. Twinning is an important deformation mechanism in many materials, but there is limited knowledge of the role of twinning in polygranular graphite and no experiment to date has investigated its occurrence in situ under load in the bulk material.

The microstructure of synthetic polygranular graphite contains a high level of thermally induced residual stress due to the strong graphite crystal anisotropy and high processing temperatures [28]. Synchrotron X-ray diffraction studies have shown that these internal stresses are relaxed upon mechanical loading [29]. Twinning, kink band formation and basal plane slip all are mechanisms by which crystals can deform in the microstructure, and local variations in residual stress are expected to affect their onset when the microstructure is subjected to additional strain.

To investigate these mechanisms, it is necessary to be able to detect changes in the orientation of crystals in the polygranular microstructure, which requires advanced diffraction techniques. Electron backscatter diffraction (EBSD) is not readily applicable to graphite due to the difficulty of obtaining an adequate surface [30]. Although grain mapping by Diffraction Contrast Tomography (DCT) has been used to provide three-dimensional grain maps of metals and ceramics [31,32], tests by some of the authors that were completed at ESRF-ID11 [33] with Gilsocarbon graphite found that it did not provide the clear diffraction spots necessary for pair-matching and grain reconstruction.

Three-Dimensional Synchrotron X-ray Diffraction (3DXRD) was developed for low-resolution crystal orientation mapping of samples with large grains (of the order of a few hundred microns) [34,35]. Ideally, the materials investigated have well-ordered crystal domains from which segmentation of the diffracted spots and pair-matching can be used to obtain 3D maps of crystal shape and dimension, such as in Diffraction Contrast Tomography (DCT). In graphite, although there are large domains (>100's of μm) of crystallites with parallel basal (0001) planes [5], these have a high degree of misorientation along [0001] [36]. Consequently, diffraction patterns of sufficient quality for 3DXRD indexing and reconstruction are not attainable. However, a simuli-3DXRD experiment may sample a gauge volume in which a strong local texture from the graphite domain structure will give partial Debye-Scherrer cones, observed as partial rings on a 2D detector. The distribution of intensity around these rings should be sensitive to changes in grain orientation (e.g., kinks or twinning) and coherence (i.e., anisotropic plastic deformation).

Bragg-edge neutron imaging is a fast-developing acquisition tool that can provide energy-resolved information of internal structures in materials, and recent

developments of in situ wavelength-dependent imaging allow accurate determination of crystal lattice strains [37,38]. A relatively unexplored use of Bragg-edge imaging is direct image processing and analysis of extinction spots for those crystals that are in the Bragg-condition. This application of energy-resolved neutron imaging is particularly suitable for materials with grains or domains over 100 μm in size as neutron detectors currently have quite low spatial resolution compared to X-ray imaging. Briefly, when the neutron wavelength is much larger than twice the interplanar spacing of the periodic crystal lattice planes, there is no coherent scattering. However, at wavelengths where the Bragg condition is satisfied by suitably oriented planes there is a marked change in the transmitted intensity (i.e., a Bragg edge) [39]. On a radiograph of a polycrystalline material at a specific energy, extinction spots with reduced intensity arise from the grains in which the neutrons have been scattered at the corresponding Bragg edge. At energies close to the Bragg edge, the intensity of these spots is most sensitive to changes in crystal orientation or changes in scattering due to the disruption of coherency by plastic deformation [40]. A recent in situ study of the deformation of Gilsocarbon graphite at the ISIS spallation neutron and muon source on the IMAT (**I**maging and **MAT**erials science and engineering) instrument observed local changes in Bragg contrast images [38]. As Bragg contrast is affected by local changes in scattering, this may provide evidence for local grain reorientation or plastic deformation [31,34,41,42].

The objective of this study was therefore to apply the advanced and in situ characterisation techniques of Bragg-edge neutron imaging and 3DXRD to investigate the crystal deformation mechanisms by which the synthetic polygranular Gilsocarbon graphite accommodates strain. The study was conducted with un-irradiated graphite at room temperature during compressive loading, as the first step towards future

investigations of the effects of neutron irradiation and elevated temperature that are relevant to its performance in nuclear engineering.

2 Experimental Details

2.1 Material

The material, supplied by EDF Energy Generation UK, is a moulded IM1-24 Gilsocarbon (GCMB grade) polygranular nuclear graphite that was manufactured by Graftech (formally UCAR). It has weakly anisotropic properties and the elastic Young's modulus is reported to be between approximately 11.6 and 11.9 GPa (Poisson ratio of 0.2), with tensile strength of ~ 20 MPa and compressive strength of ~ 75 MPa [43]. It is one of the graphite grades used in the core of the UK Advanced Gas-cooled Reactor fleet. The specimens, prepared using Electrical discharge machining (EDM), are presented schematically in Figure 1 with their loading methods.

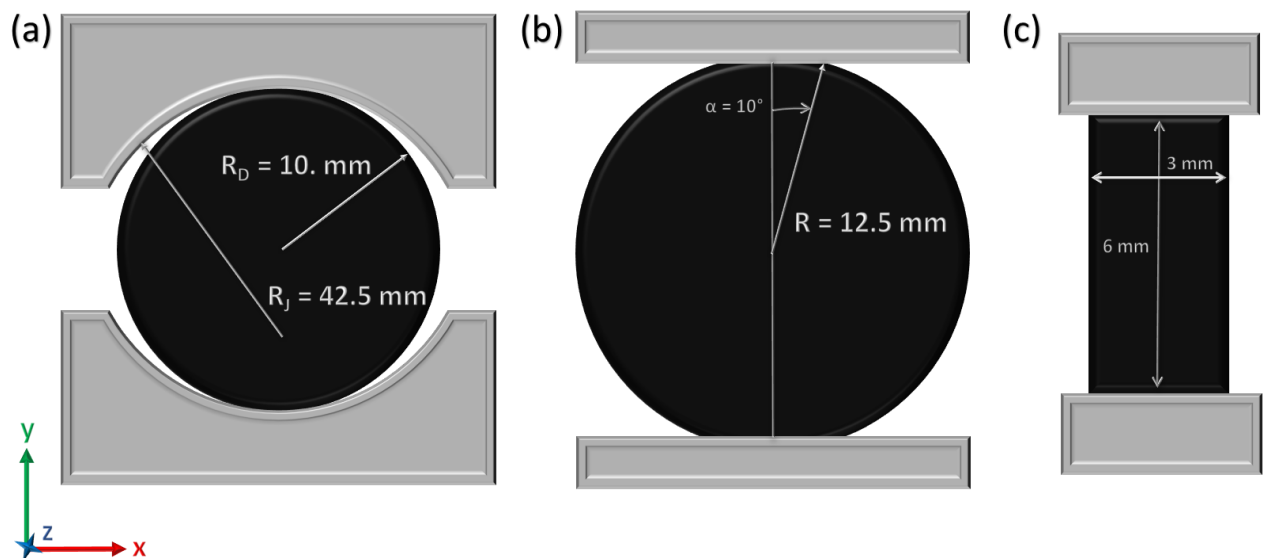


Figure 1: Schematic of specimens A (a), B (b) and C (c), all loaded in compression along the vertical y-axis

2.2 Energy-resolved Neutron Imaging

The in-situ neutron Bragg-edge imaging experiment took place on the IMAT beamline at the STFC-ISIS facility under experiment number RB1910517-2 [44]. Except where noted, it followed the setup and analysis described in the previous method paper [38]. The pinhole aperture and the neutron count (exposure time) were optimised to

increase the counting statistics and the Signal-to-Noise Ratio (SNR). Two specimens of slightly different geometry were investigated (Figure 1 a and b). Specimen A was a round disc (20 mm diameter, D , × 10 mm thickness, T) that was manually loaded across its diameter using curved steel anvils (radius 42.5 mm) with a relative curvature to the specimen of $\rho = 0.24$, which is in line with recommendations for diametral compression testing of brittle materials [45]. Specimen B adopted a slightly larger size disc design (25 mm diameter, D , × 12.5 mm thickness, T), with diametrically opposed flattened surfaces (width 4.26 mm) for a contact angle 2α of 20° . This was loaded in compression across its diameter using flat steel anvils. Both designs avoid premature failure from contact stresses [46,47], but have respective challenges of matching the anvil curvature to the deforming disc and ensuring parallelism of the flat surfaces.

The count current per scan that is the total neutron exposure (i.e., accounting for temporary loss of beam) for specimen A was 240 μA (approximately 6 hours per scan), which was twice that of the previous proof-of-concept experiment [38]. Due to time constraints, the count current for specimen B was 120 μA (3 hours, same as proof-of-concept) but the dataset quality was improved at the expense of spatial resolution [38] by increasing the pinhole aperture from 40 mm to 60 mm. The 28×28 mm Micro-Channel Plate (MCP) neutron detector [48] with 2×2 Timepix ASICs for readout (256 × 256 pixels each), for a total array of 512 × 512 pixels, with a spacing of about 3 pixels between each chip was used. For specimen A, the Bragg-edge image resolution was 168 μm . The image resolution was approximately 276 μm in the configuration for specimen B due to an increase in the detector distance (to accommodate the driving screw of the loading rig) in addition to the effect of the larger pinhole aperture. Example radiographs at the same wavelength close to the (0002) Bragg edge are given in the Supplementary Information.

Both specimens A and B were observed at a reference preload (110 and 200 N respectively), then with in situ observations during loading and unloading. The changes in radiographs at energies near to the (0002) Bragg edge, relative to the preload radiograph, were extracted using the method developed in [38]. Briefly, the datasets were pre-processed in BEAn [49] and analysed in NEUTRONIX [50][36]. A digital image correlation (DIC) algorithm was applied to radiographs at energies away from the Bragg edge (i.e., with image contrast dominated by attenuation due to density changes from internal pores). This provided 2D displacement fields of the specimen's movements and deformation, which was used to precisely register and transform the radiographs that were recorded at energies near to the (0002) Bragg edge. It was then possible to map, via subtraction, the residual difference between Bragg edge radiographs of the deformed image and the unloaded reference at the same locations in the specimen in order to detect local changes in neutron scattering.

2.3 Three-dimensional X-ray Diffraction and Tomography

The experiment was completed on beamline ID11 at the European Synchrotron Radiation Facility (ESRF) under experiment number ME1504 [33] in Experimental Hutch 3 (EH3) with a monochromatic beam (40 keV) obtained using a Laue-Laue double bent silicon crystal monochromator. Specimen C (Figure 1c) was a cylinder (6 mm length, L , 3 mm diameter, D) that was loaded by compression along its longitudinal axis. For 3DXRD, a gauge window with a slit opening of $300 \times 300 \mu\text{m}$ was centred on the longitudinal axis of the specimen, and the Far Field detector FReLoN-4M was used to collect diffraction patterns at 1° intervals (each with an exposure time of approximately 0.15 s) over a full 360° rotation. Following this 3DXRD acquisition, the scintillator of the Near Field FReLoN detector was placed in the beam and the slits were opened to approximately $3 \times 3 \text{ mm}$ for tomography (XCT) at $1.5 \mu\text{m}/\text{voxel}$. The

tomographs ($2,000^3$ voxels) were reconstructed using pyHST2's Paganin reconstruction routine [51].

Specimen C was loaded in steps of ~ 40 N to a maximum of 300 N (~ 42 MPa compressive stress) and then unloaded in steps of ~ 50 N. Each loading step was followed by a wait time of a few seconds to stabilise the load before acquiring data by 3DXRD and then XCT. Alternate loading steps placed the Field of View (FoV) in the centre of the specimen (ROI-A, reference pre-load 5.4 N) and then with the FoV centre translated horizontally along the cylinder radius by about $200 \mu\text{m}$ (ROI-B, reference pre-load 50 N).

Local Digital Volume Correlation (L-DVC) of the tomographs in LaVision DaVis (Version 8.4.0 66797) was used to extract three-dimensional displacement fields to quantify the movement and deformation of specimen C. The correlation approach prioritised precision and accuracy of the measurements over spatial resolution. A Fast Fourier Transform (FFT) DVC was used at a final subset size of 256^3 voxels, with a search radius of 16 voxels, followed by a 4-step Direct Correlation (DC) at 64^3 voxel subset size at 75% overlap.

Changes in the crystal orientations in the 3DXRD gauge volumes of ROI-A and ROI-B were quantified by examining the effect of the specimen rotation on the azimuthal variation of intensity in the 2D images of the (0002) Debye-Scherrer diffraction rings. The variation of intensity with azimuth angle, χ , depends on the texture of the diffracting crystallites in the gauge volume that defines the ROI, and changes in the texture will change the azimuth angle, χ_m , at which there is maximum intensity. Similarly, a change in the texture or orientation of the crystals will change the stage rotation angle, Φ , at which their Bragg diffraction condition is satisfied. The Bragg

angle of the (0002) reflection at 40 keV is small (2θ is 5.1 degrees), so for small angular changes in the crystal orientation the change in Φ that is required to bring the crystals back into diffraction is similar. Peak fitting and interpolation techniques were used to determine the rotation angle, Φ , of the maxima in azimuthal angle, χ_m , of maximum intensity with sub-degree resolution. The change in Φ was tracked in each ROI as the compressive load was increased and then decreased in order to study the changes of orientation of the crystal domains in the ROI gauge volume. The analysis methods are described in more detail in the Supplementary Information.

3 Results

3.1 In Situ Bragg-edge neutron imaging

Total strains in the vertical x - y plane were mapped for both specimens using Digital Image Correlation (DIC) on neutron radiographs obtained at energies away from the Bragg edge, as described in [38]. Specimen A was a round disc loaded with curved anvils, for which the closest standard [52] advises equation (1) for calculating the tensile stress, σ_t , acting at the centre of the disc due to the compressive applied load, P_{frame} :

$$\sigma_t = \frac{P_{frame}}{TD} \times Y \quad (1)$$

The ratio of disc radius to anvil radius, ρ , is an important factor that determines the constant, Y , but its sensitivity to ρ (here 0.24) is not significant in the range 0 to 0.67 [45]. Equation (1), where $Y = 0.636$, leads to a result within 7% of the ASTM (American Society for Testing of Materials) standard D8289–19 [53] that is derived from Hondros [54]. For point loading of the disc, the ratio, k , of the magnitudes of the compressive, σ_c , to tensile, σ_t , stresses at the disc centre is 3 [55,56], which is also correct for small angles of load contact [54]. With the disc/anvil ratio ρ used here and elastic contact with graphite's Young's modulus of ~11 GPa [5] the contact semi-angle remains less than 6° and the biaxiality is within 2% of $k = 3$ [57]. Specimen B was a flattened Brazilian disc, loaded between flat, parallel platens. It is best described by the ASTM standard D3967-16 [58], where the tensile stress, σ_t , at the specimen centre is calculated with equation (2) and finite element analysis has shown that for contact angle $2\alpha = 20^\circ$ the coefficient $Y(\alpha) = 0.964$ [47,59,60].

$$\sigma_t = \frac{2P_{frame}}{\pi TD} \times Y(\alpha) \quad (2)$$

Given the semi-angle for the flattened disc of 10° is constant and $<15^\circ$, we make the same approximation that $k = \sigma_c/\sigma_t = 3$.

Figure 2 maps the component of normal strain, ε_{yy} , parallel to the diametral loading direction for specimen A, calculated from the DIC-measured displacement field by Least Square Matching (LSM) at 69 pixel per subset and a step size of 3 pixels and relative to the preloaded reference. The load was increased from i) to iv), with a partial unload and then reload shown in v) and vi). Large compressive strains at the contact points are visible. Figure 3 presents the evolution of the average value of ε_{yy} in a central gauge area (approximately 4×4 mm) for both specimens A and B, where the biaxial strain state is quite uniform [61]. Both samples show essentially elastic loading. They have a similar relation between the average strain and change in compressive stress, with some apparent hysteresis. Their behaviour is not quite identical, which may be due to the effects of nonlinear deformations near the loading surfaces in the two specimen geometries. A least-squares fit to the mean values in Figure 3b has a gradient of 12.10 ± 0.44 GPa.

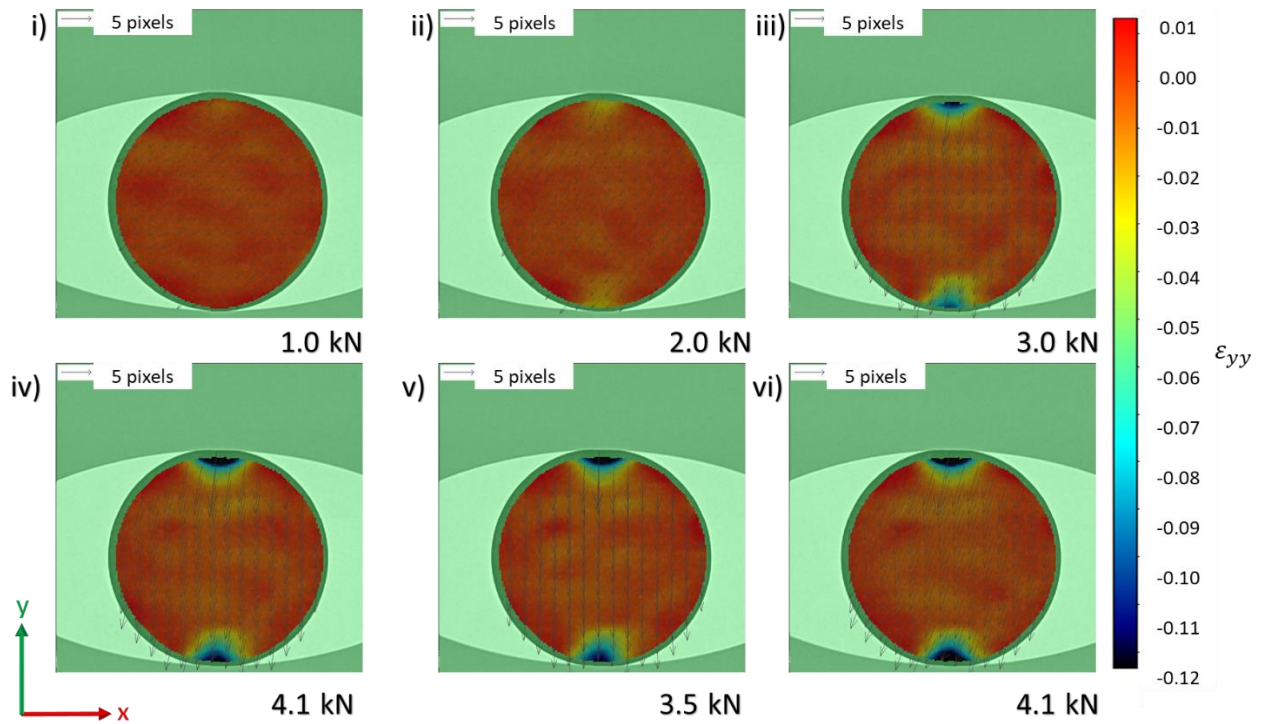


Figure 2: Specimen A: maps of the strain ϵ_{yy} parallel to the vertical loading direction measured by DIC of radiographs with varying load from i) to vi). The colour scale is the strain. The arrows show the local displacements relative to the preload and are not corrected for rigid body translation or rotation. The arrow length is proportional to the displacement magnitude (1 pixel = 55 μm).

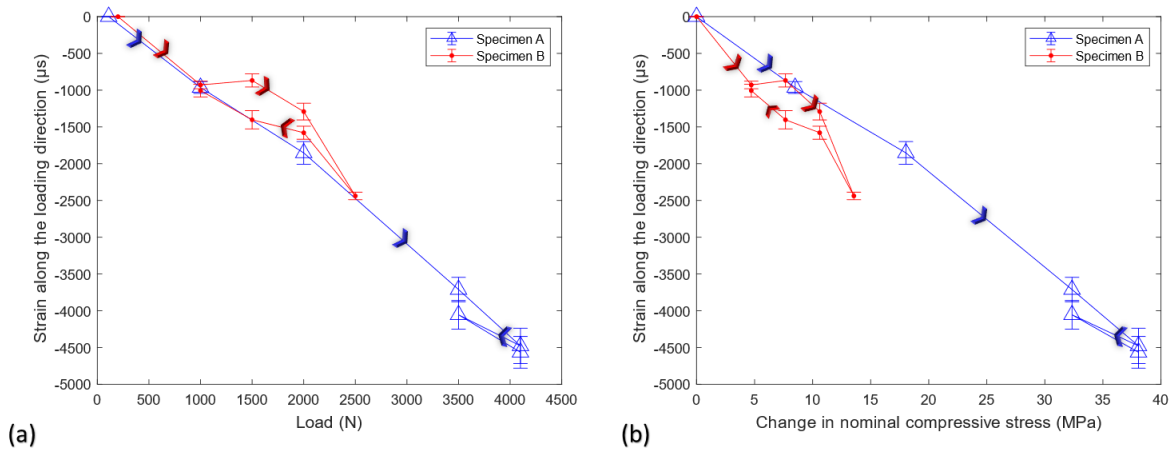


Figure 3: Average strain ϵ_{yy} , measured by DIC at the centre of specimens A and B with loading and unloading as a function of a) load; b) change in compressive stress. The strain error bars represent the 95% confidence in the mean (sample size 200 measurements in 4x4 mm gauge area). Points have been added to indicate zero strain at the pre-load (i.e., zero stress change). Green arrows indicate the load/unload sequence

The example Bragg edge radiograph residuals for specimen B (Figure 4a, with zoomed images of a selected region in Figure 4b) show a pattern of extinction spots (dark) and loss of extinction (bright) due to local differences in the (0002) Bragg edge diffraction between the reference (preload) and loaded states. Some extinction spots remain practically constant with load - e.g. compare Figure 4b i) with Figure 4b iv) in the solid circled area. Others disappear and then reappear as they enter and leave the Bragg condition with increasing and then decreasing load - e.g. compare Figure 4b i) with Figure 4b ii) in the dash-dot circled areas, and then Figure 4b vi). Similarly, bright spots arise from regions that were in extinction in the reference image and are no longer coherently scattering in this condition under load - e.g. compare Figure 4b i) with Figure 4b ii) in the dotted ellipse. Similar behaviour was observed in Specimen A (the residual Bragg edge radiograph maps are presented in supplementary information).

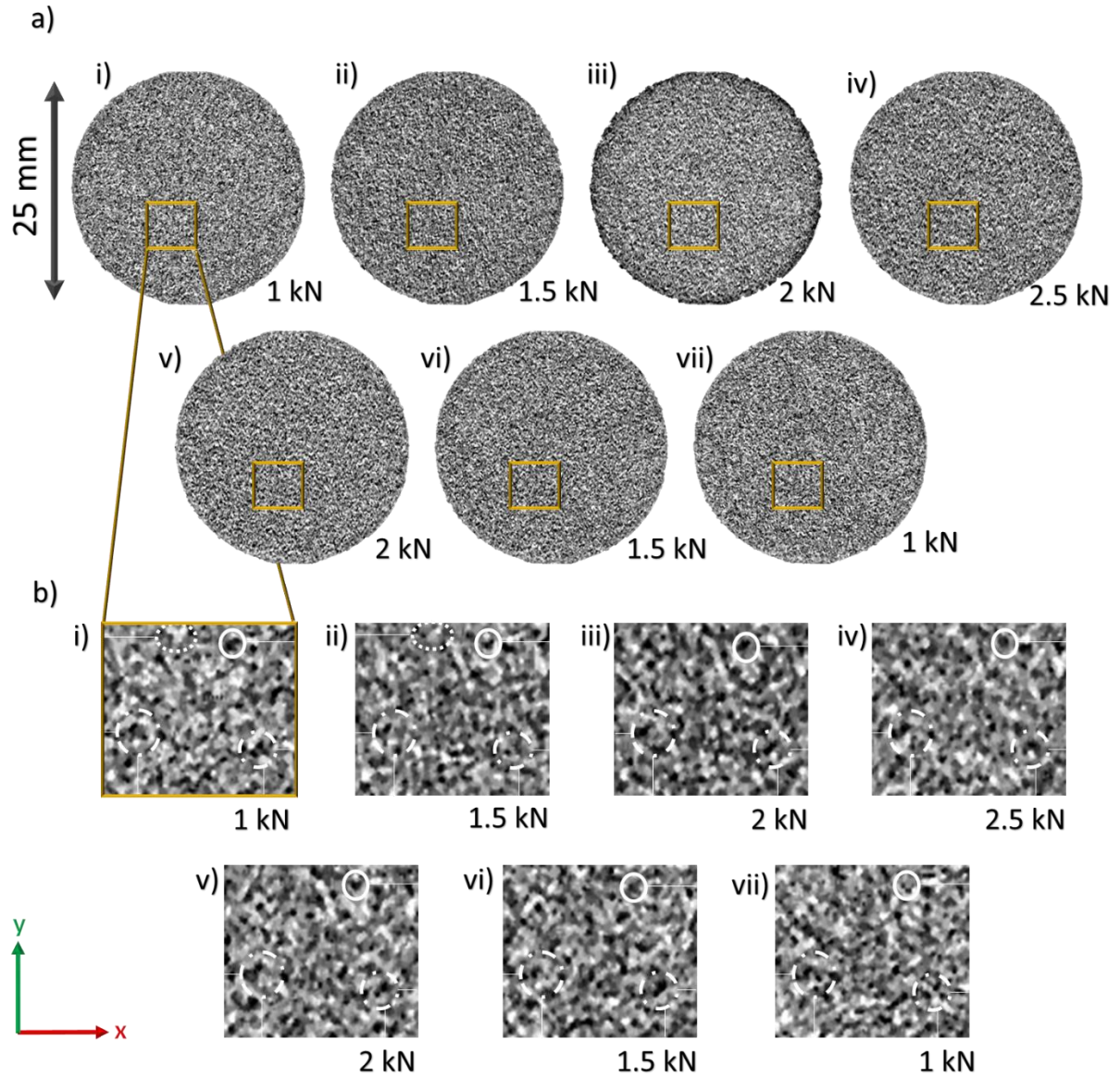


Figure 4: Specimen B: (a) radiograph residuals at the (0002) Bragg edge, relative to the preload, with increasing load to 2.5 kN, then unloading to 1 kN. The marked area of interest is shown with higher magnification in (b), where the dash-dot/solid circles and dotted ellipse identify selected extinction spots that are described in the text

A further DIC analysis was applied to quantify the changes between the maps of the Bragg edge radiograph residuals by determining their level of correlation relative to one loaded state. The analysis used the Davis Strainmaster 8.4 software, with a Least Square Matching algorithm at a step size of 3 pixels and a final subset size of 69 pixels, (an outlier filter and 5x5 Gaussian smoothing were applied). High correlation would indicate persistence of the local pattern of image contrast with change in load, whereas low correlation would arise from significant differences, due either to random image noise or a change in the local scattering within the microstructure. Figure 5 presents maps of the correlation coefficient for the residual radiographs of specimen A and specimen B. The first residual map (at 1 kN) was used as the reference for correlation in each case. The high levels of correlation show that many of the dark or bright spots are persistent between the images, as was observed in the preliminary proof of concept study [38].

For both specimens, Figure 5 shows there is an apparent decrease in the correlation values as the compressive load magnitude is increased, and higher correlation values on unloading. **Error! Reference source not found.** This is quantified in Figure 6 using the median value of the correlation coefficient (values of 0 or NaN excluded) for the data within the central 4 × 4 mm ROI gauge area. The correlation coefficient values may be affected by differences in data noise for the imaging conditions of the two specimens. Nonetheless, both specimens show a slight decrease in the median correlation coefficient with increasing compressive load and a significant recovery (i.e. increase) when the load is reduced (Figure 6a). Figure 6b presents the same median correlation coefficient data against the change in mean compressive strain within the ROI (from the strains presented in Figure 3b) relative to the mean strain at the reference state. Both specimens show similar behaviour, where the correlation

coefficient decreases slightly with increasing compressive strain change and increases significantly as the compressive strain is reduced.

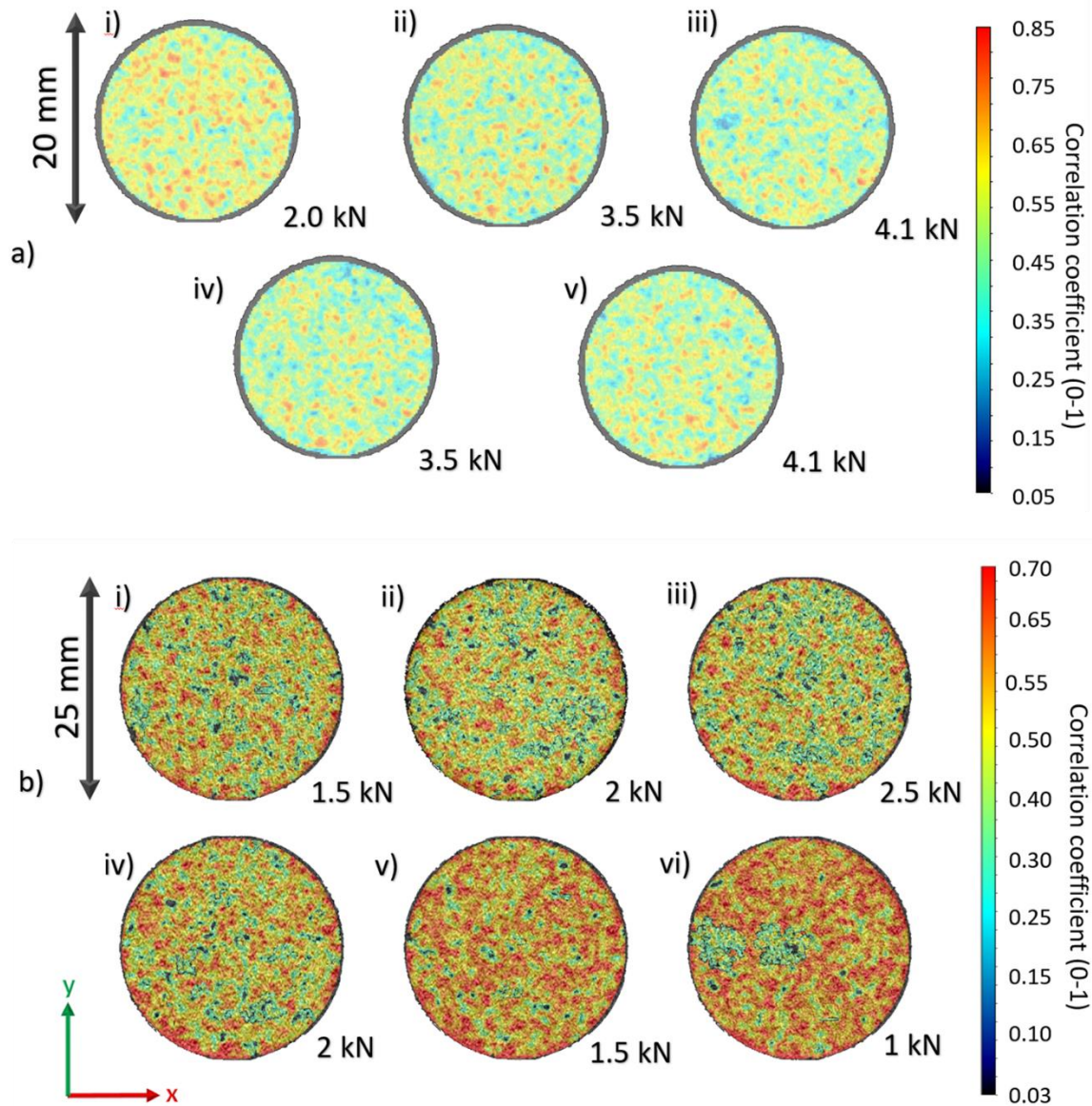


Figure 5: Maps of the correlation coefficient between the (002) Bragg edge radiograph residuals (relative to the map at 1 kN): a) Specimen A with i) to iii) compressive loading (along the y-axis), iv) partial unload and v) reload, and b) Specimen B with i) to iii) compressive loading and iv) to vi) unloading

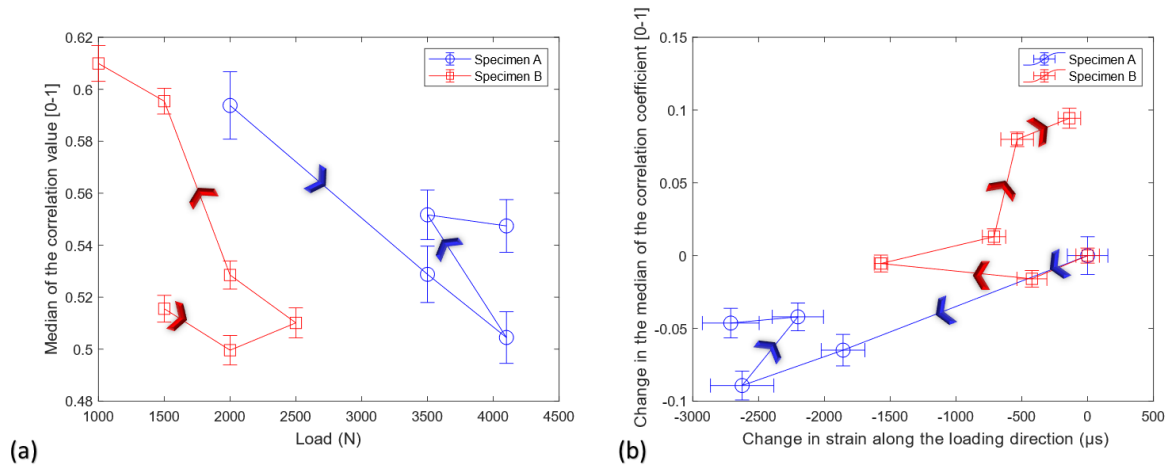


Figure 6: The median of the correlation values (from Figure 5) for Specimen A and Specimen B, in the central 4 x 4 mm ROI gauge area as a function of a) applied compressive load; b) change in mean strain ϵ_{yy} (measured by DIC in the ROI) relative to the reference. The green arrows show the sequence of the loading. Error bars are 95% Confidence Interval in the median for the correlation value.

3.2 In Situ Three-Dimensional Synchrotron X-ray Diffraction

3.2.1 Total and elastic strains

There were no microstructure changes nor damage visible in specimen C in response to loading. Example sections of high-resolution tomographs of ROI-A at the preload and maximum load are shown in Figure 7. The change in elastic strain within the graphite crystals (XRD) was obtained from the relative shifts of the (0002) peak, as in [61]. The 2D diffraction pattern (e.g. Figure 9a) was azimuthally caked in 1° bins, cross-correlated with the preload pattern to measure the peak shifts and the results fitted to obtain the 2D strain tensor (details are provided in the supplementary information). The results are presented in Figure 8a for both radial, ε_r^{XRD} , and longitudinal (compression, ε_{yy}^{XRD}) strains. The compressive behaviours of ROI-A and ROI-B are similar and appear elastic with no significant difference between loading and unloading. The transverse radial strains, ε_r , are tensile. The ratio of the gradients of transverse to longitudinal strains with applied load is 0.19 ± 0.7 . Although the uncertainty is large, this is close to the Poisson's ratio of Gilsocarbon [5,29].

The DVC analysis of the tomographs used the attenuation contrast due to microstructure porosity and density variations, achieving correlation coefficients above 0.7. The average longitudinal compressive strains (ε_{yy}^{DVC} , measured using the best fit to the local gradients of the displacement field across the analysed ROI) are presented in Figure 8b as a function of the change in magnitude of the compressive longitudinal stress. The behaviour appears elastic, and a fit to the combined data for stress vs. ε_{yy}^{DVC} from ROI-A and ROI-B (for both loading and unloading) gives an apparent Young's modulus in compression of 9.16 ± 0.67 GPa. The precision of the DVC analysis did not allow meaningful measurements of the transverse strains. Figure 8c presents the relationship between the longitudinal total strain (DVC, ε_{yy}^{DVC}) and elastic

(XRD, ε_{yy}^{XRD}) strain in compression for both ROI. A linear fit to the combined data has a gradient ($\varepsilon_{yy}^{XRD} / \varepsilon_{yy}^{DVC}$) of 0.26 ± 0.02 .

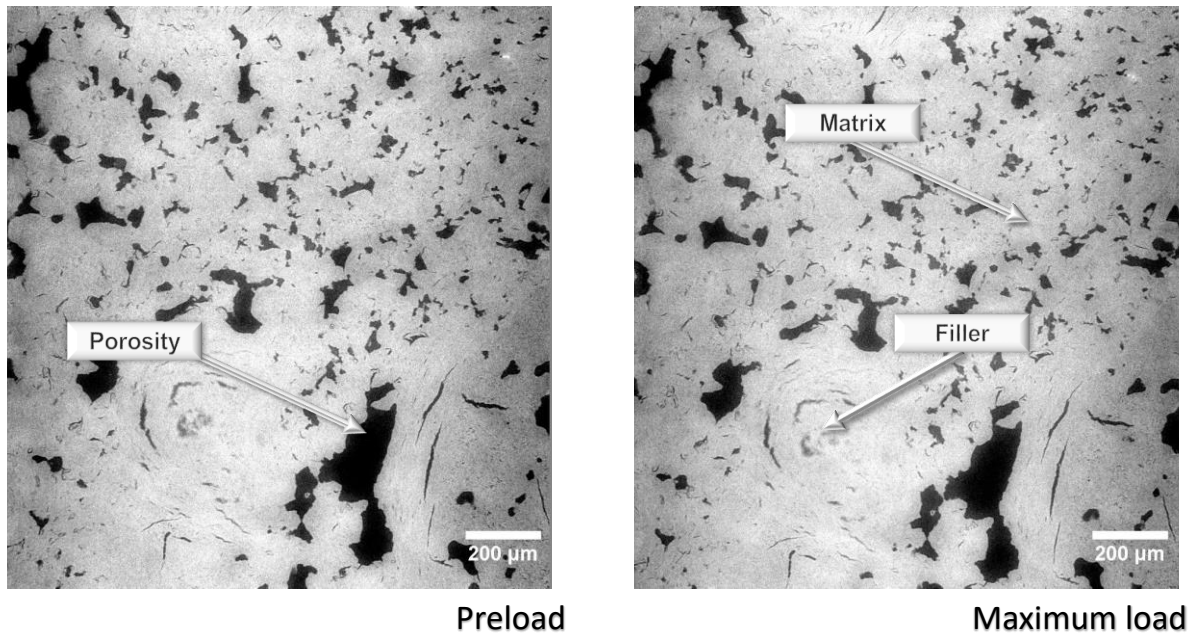


Figure 7: Example tomography slices (vertical sections) at preload (1 MPa) and maximum load (~40 MPa) for ROI-A in Specimen C. The compressive loading direction was vertical. Typical features of a coarse Gilsocarbon filler particle, matrix and porosity are identified.

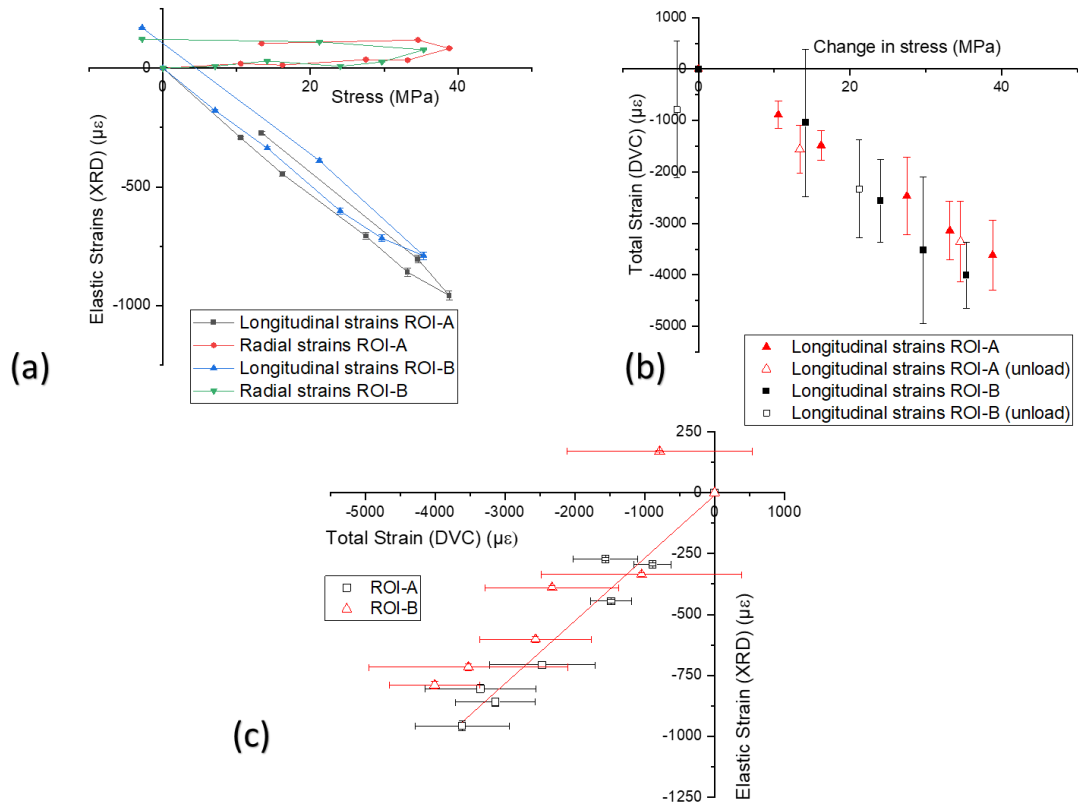


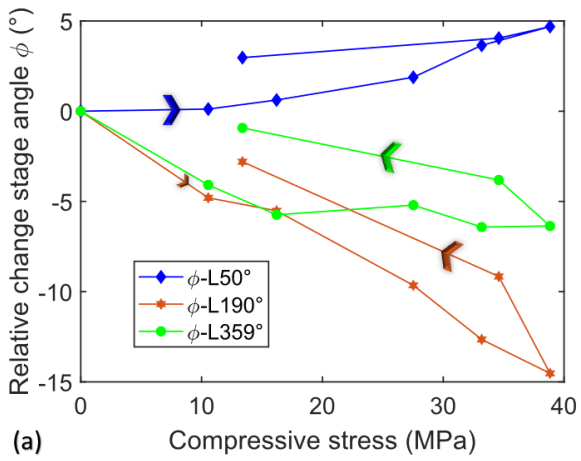
Figure 8: Strain measurement in both Regions of Interest (ROI-A and ROI-B) during axial compression of Specimen C: a) change in strain measured by XRD (radial ϵ_r^{XRD} and longitudinal ϵ_{yy}^{XRD}) with the change in compressive stress (relative to the preload state); b) change in strain measured by DVC (longitudinal ϵ_{yy}^{DVC}) with the change in compressive stress; c) comparison between the longitudinal strain changes measured by DVC (ϵ_{yy}^{DVC}) and XRD (ϵ_{yy}^{XRD}).

3.2.2 Crystal Orientation Tracking

An example diffraction image obtained at one rotation angle is shown in Figure 9a. The contrast has been enhanced in Figure 9b to show two regions of the (0002) Debye-Sherrer ring that have higher intensity at symmetric (high and low) azimuth angles ($\chi - H$ and $\chi - L$). These regions, which are due to texture of the crystal domains, were analysed independently. The DVC analysis (see Supplementary Information) found the movements of the specimen were less than 50 μm at the highest load. This is small in comparison to the 300 μm slit size used for the diffraction acquisitions, so the sampled ROI for 3DXRD was essentially constant throughout the observations. The physical rotations were less than 0.3° up to the maximum load.

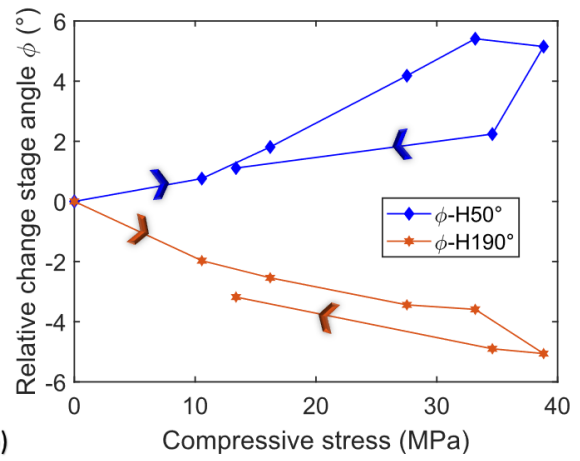
The azimuth angle, χ_m , at which there was a maximum intensity around the (0002) Debye-Sherrer ring varied with the rotation angle of the stage, Φ , to give a series of peaks (Figure 9c) due to different crystal domains within the gauge volume. Each peak is labelled by its azimuth position (high H or low L) and by the approximate angle Φ (rounded to five) of the stage rotation for the peak (e.g. $\Phi - L50^\circ$). Analysis of the χ_m vs Φ relationship was used to identify and fit, with sub-degree precision, the stage angle, Φ , of the major peaks. This allowed measurement of the angular change in peak position, $\Delta\Phi$, with applied compressive stress. Further details of the analysis are in the Supplementary Information.

Results from ROI-A

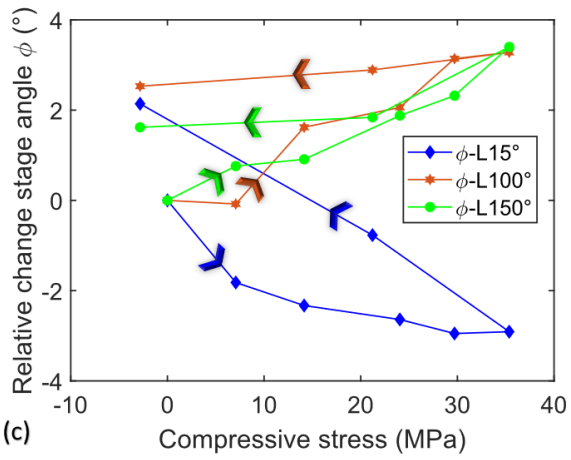


(a)

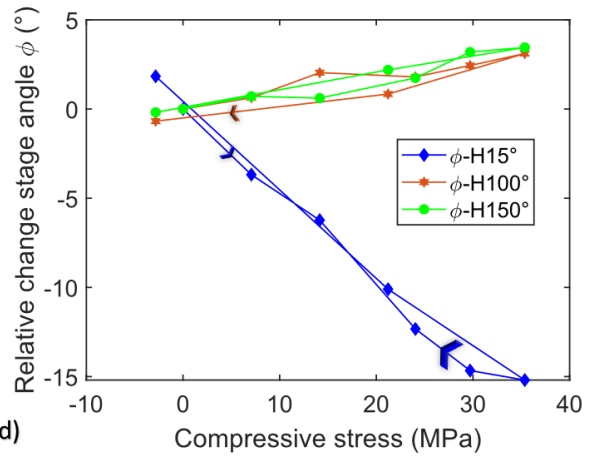
are shown in



(b)



(c)



(d)

Figure

10a

and

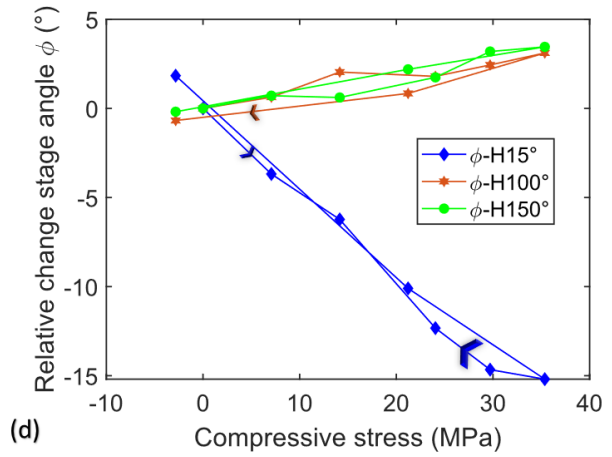
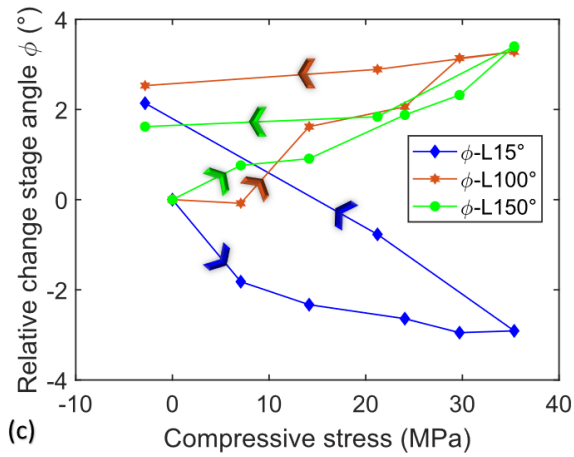
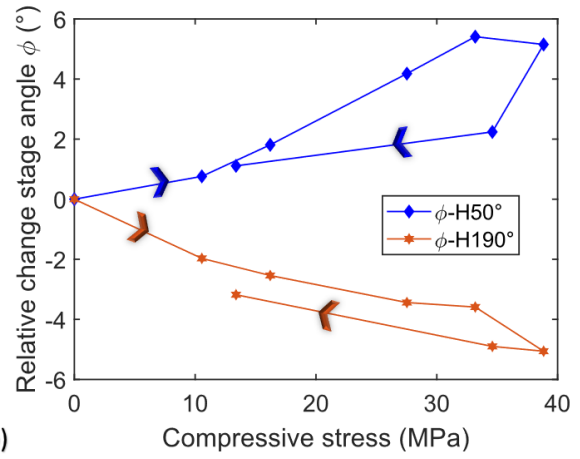
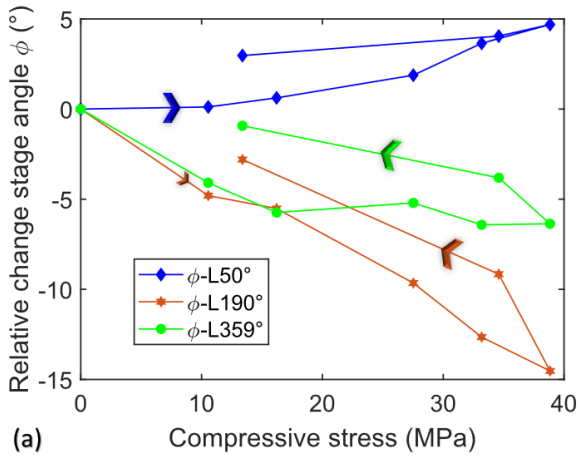
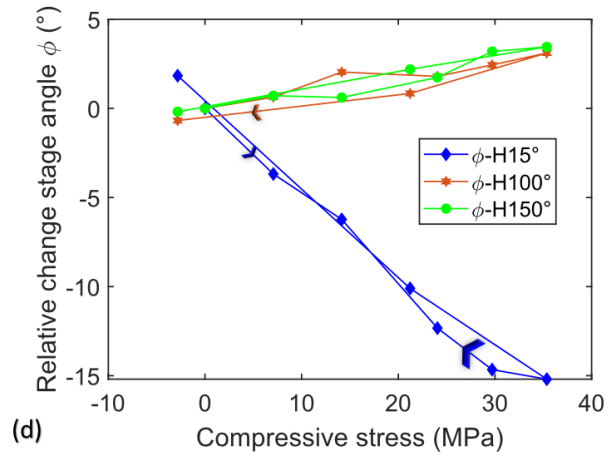
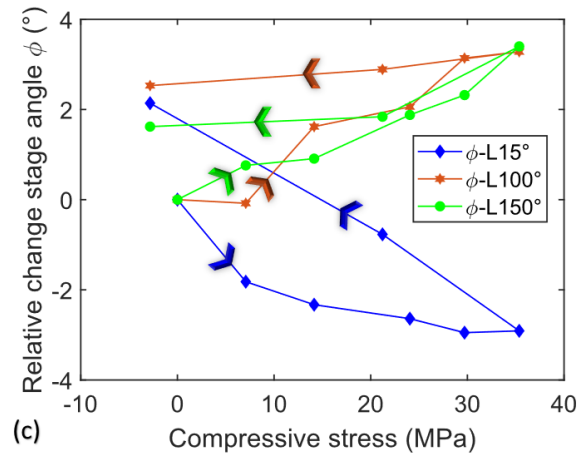
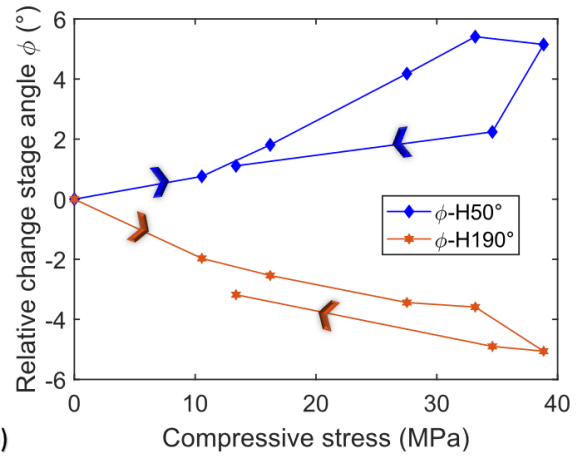
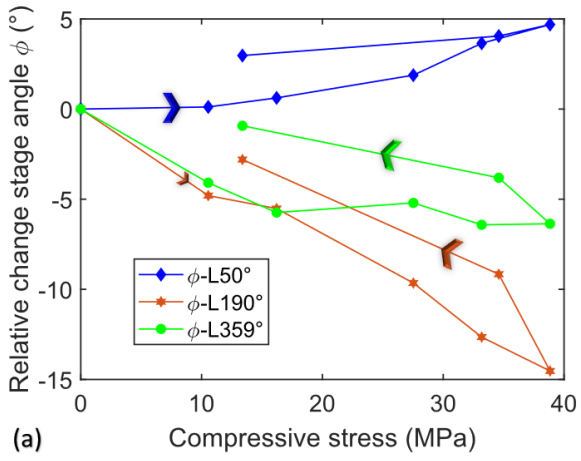


Figure 10b for several sets of azimuth peaks. No new peaks were observed with change in load. It was not always possible to track the same H and L pairs (e.g. $\Phi - L190^{\circ}$ and $\Phi - H190^{\circ}$), nonetheless the figure shows opposing trends for such pairs as the angular peak positions varied systematically with the compressive stress.



Figure

10c

and

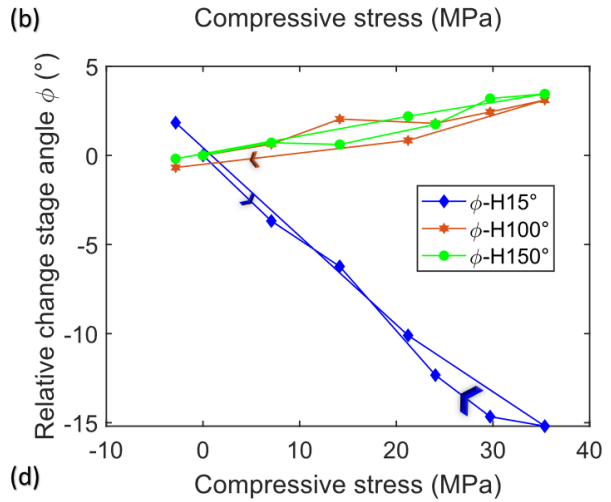
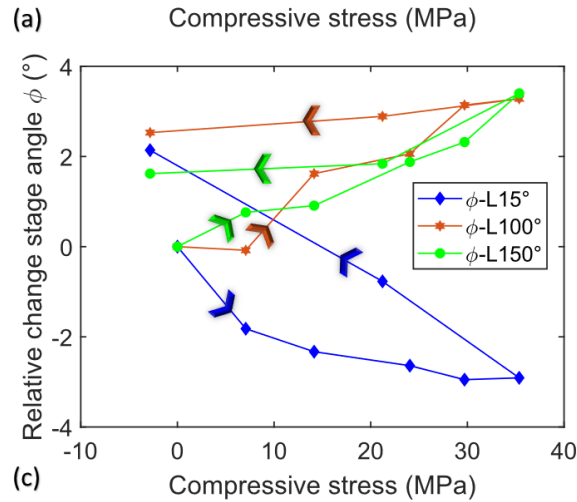
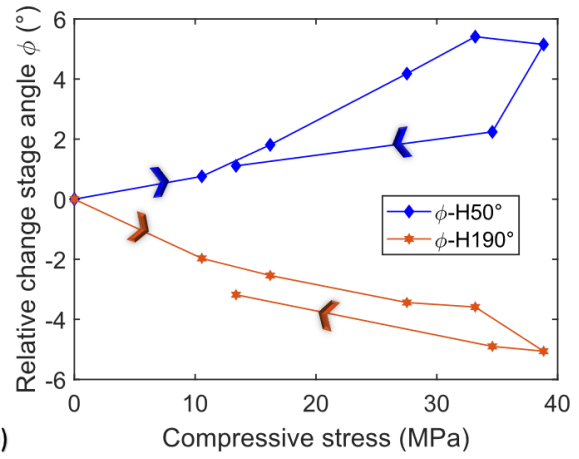
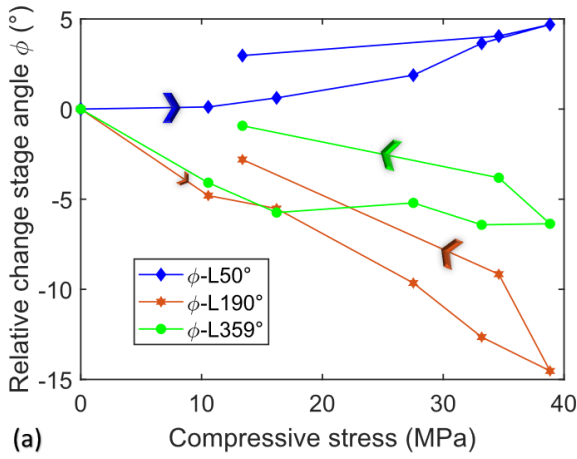


Figure 10d present data for ROI-B, which showed similar behaviour. The angular changes were not always fully recovered as the stress was removed. The magnitudes of the angular change, $\Delta\Phi$, differed between peaks, and also between ROI-A and ROI-B. The angular changes were significantly larger (typically by up to at least an order of magnitude) than the physical rotations of the specimen.

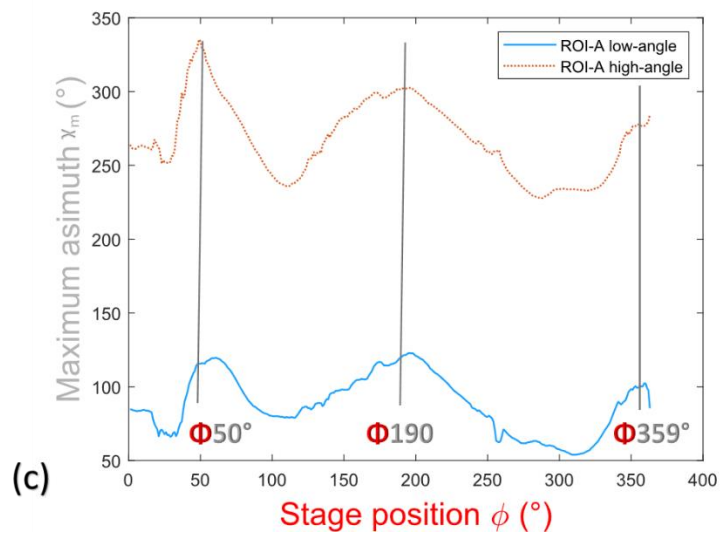
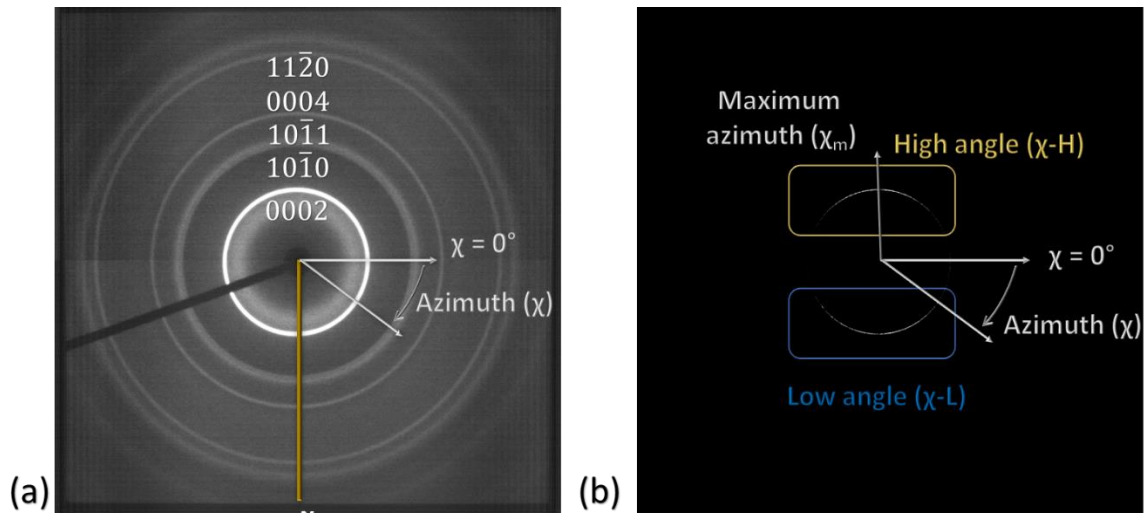


Figure 9: Example analysis of the 3DXRD data for Specimen C: a) image of the Debye-Scherrer rings at one stage rotation angle, Φ ; b) enhanced contrast to identify the $\chi - H$ and $\chi - L$ regions of the (0002) ring with higher intensity; c) variation of the azimuth angle of maximum intensity (χ_m) of the low angle $\chi - L$ and high angle $\chi - H$ region of ROI-A as a function of stage rotation angle, Φ , to identify various peaks, $\Phi - L50^\circ$, $\Phi - L190^\circ$ etc. The change of Φ for each peak ($\Delta\Phi$) with applied stress was then determined by peak fitting.

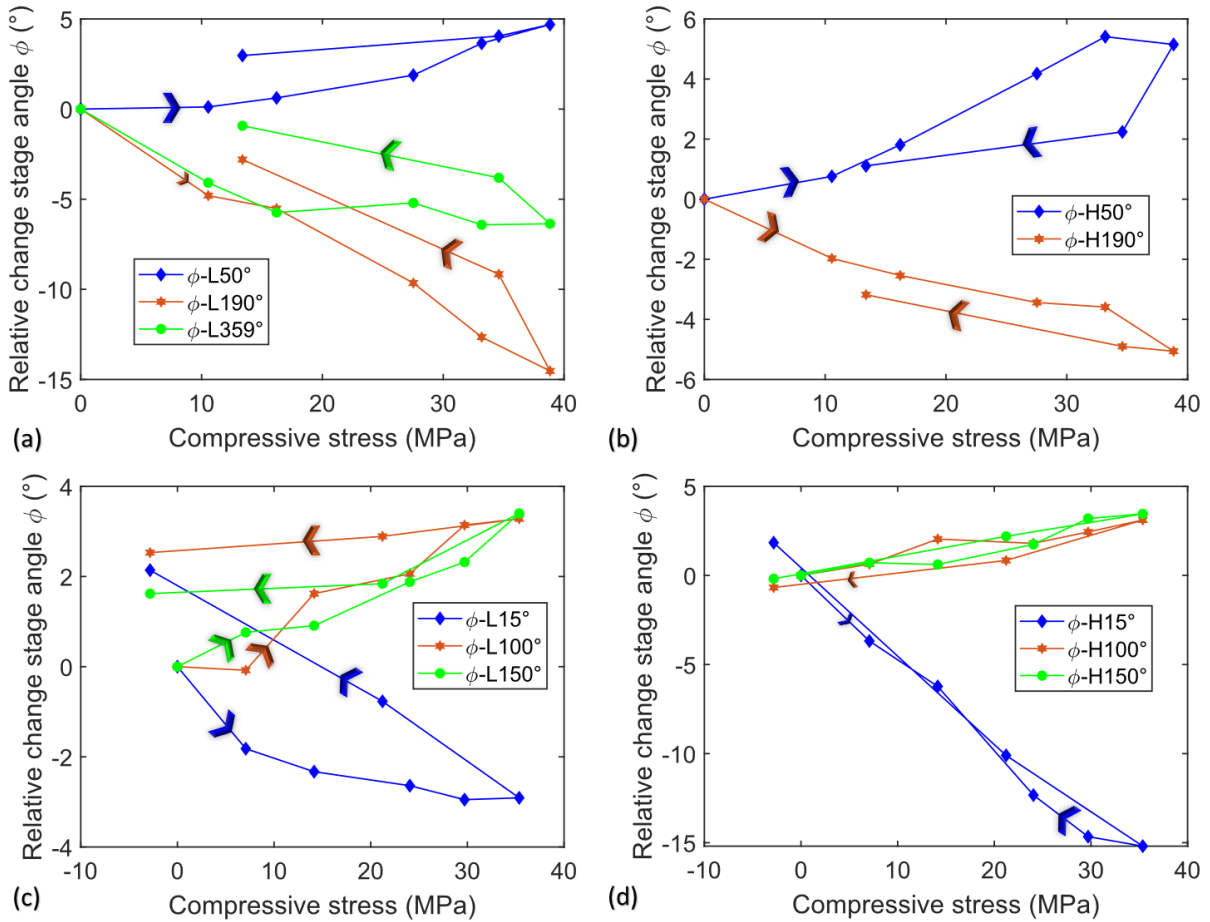


Figure 10: The relative change in stage rotation angle, $\Delta\Phi$, for maximum intensity for selected (0002) peaks at high H and low L azimuth angles as a function of the change in compressive stress, for both ROI-A (a and b) and ROI-B (c and d). The cumulative fitting error is below 5% for all peaks tracked. Nominal points have been added to indicate the reference at the origin. The arrows represent the direction of loading.

4 Discussion

Both disc compression specimens (A and B) showed similar elastic behaviour in compression, with some apparent hysteresis with unloading, and an effective Young's modulus of 12.10 ± 0.44 GPa (Figure 3). The axially compressed specimen in the 3DXRD study, loaded over the same range of compressive stress as the disc compression specimens, had similar Young's modulus (9.16 ± 0.67 GPa) (Figure 8b). These moduli are lower than the value of ~ 15 GPa measured in tensile loading of the same graphite [29] but close to the expected value (10.8 GPa) of the Young' modulus for Gilsocarbon graphite [62]. The differences between the moduli of the specimens may be due to material heterogeneity and small specimen size, and also the effect of the non-linear deformation of graphite on the determination of stress and strain in different specimen geometries.

The XRD analysis in this work has measured the change in the (0002) crystal lattice periodicity in order to determine the elastic strains acting perpendicular to the basal planes. The graphite crystal has very large elastic anisotropy and is most compliant perpendicular to the basal plane with an elastic modulus, C_{33} , that is typically reported as 36 GPa [5], although the value of C_{33} of defect-free monocrystalline graphite may exceed 45 GPa [63]. In the longitudinal compression specimen, the variation with applied stress of the elastic strain, ε_{yy}^{XRD} , gave an effective diffraction modulus of 26.2 ± 0.6 GPa (Figure 8a). The elastic strain was a fraction (0.26 ± 0.02) of the applied compressive strain, ε_{yy}^{DVC} , (Figure 8c). An XRD analysis of the compressive strains at the centre of a diametral compression specimen of the same Gilsocarbon graphite [57] found a similar fraction of the elastic crystal strain to total strain (0.16 ± 0.09). By inspection of the data, with calculation of stress via equation (2) and $k = \sigma_c / \sigma_t = 3$, its effective diffraction modulus for loading in compression was 44.1 ± 6.5 GPa.

The measurements discussed above were obtained during progressive loading. Measurements during unloading of a tensile specimen of the same graphite found a significantly higher diffraction modulus of 61.2 ± 6.1 GPa [64], which is quite close to the average modulus expected for a random isotropic distribution of crystals (i.e., $\pi/2 \times 36$ GPa). Polygranular graphite is a porous network of connected crystalline domains of different orientations [16]. The significant difference between the crystal strains and bulk strains (i.e. the diffraction and Young's moduli) is too large to be accounted by the 20% porosity of the Gilsocarbon graphite [17]. This shows that non-linear deformation in the microstructure affects the development of the crystal strains during loading. This is not fully reversible, since the disparity between the diffraction moduli during loading and unloading shows there is a greater contribution to the microstructure's accommodation of applied strain during loading than is recovered during unloading.

This study is concerned with mechanisms for the accommodation of strain. The analysis of the *in-situ* energy-resolved neutron radiographs showed a systematic loss of correlation with increasing load between registered radiographs taken close to the (0002) Bragg edge (Figure 6). This represents a change in the pattern of image contrast due to changes in diffraction. Such local effects would be caused either by variations in grain orientation (i.e., texture change) or coherence (i.e., non-basal plane plastic deformation), and occurred in regions with a size of the order of several pixels (i.e. 100's of μm) (Figure 4). The correlation increased as the load was removed, as the patterns of contrast become more similar to the reference. There was no clear relation between the spatial distributions of the correlation and the strain (Figure 5), although the median correlation coefficient clearly varied with applied strain (Figure 6). This may be due to relatively low gradients of strain in both specimens, except

close to the anvil contacts, and the large correlation subset size (~3.8 mm) that was required due to data noise, which would be insensitive to the short-range strain gradients. These observations show that the mechanisms that caused the changes in local diffraction are i) affected by stress; ii) at least partially reversible; and iii) occur within regions that have a size of the order of the crystal domains in the graphite microstructure.

The neutron Bragg-Edge data had a large Field-of-View (FoV) that allowed many grains to be studied. The 3DXRD method used a smaller FoV (300 μm) that was of similar size to the extinction spots. This studied a gauge volume comparable to the scale of the Gilsocarbon microstructure (Figure 7), and so examined the combined behaviour of several domains of graphite crystals. The 3DXRD observations showed there were changes of the averaged direction, or orientation vector, of the diffracting crystal domains within the gauge volume with change in applied stress (

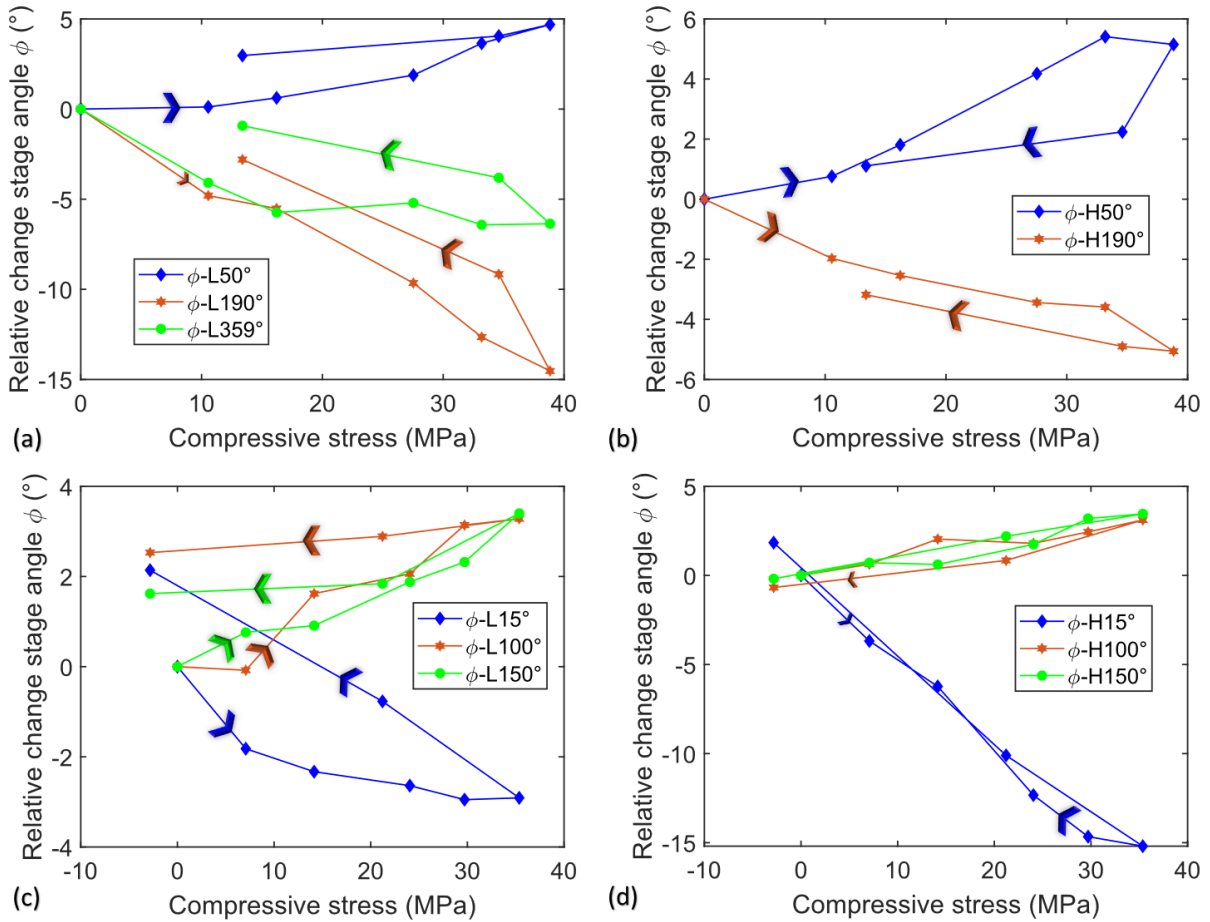


Figure 10). The change varied for different domains in the two regions of interest that were studied. Some domains deformed elastically, leading to small recoverable changes in orientation of the crystals that increased and then decreased with load. The magnitude of this elastic reorientation would depend on the domain orientation, accommodation porosity and the local stress state in the heterogeneous microstructure. The reorientation was larger in some domains and was not fully recovered on unloading, which shows that inelastic behaviour occurred.

Both the neutron and X-ray observations show that non-linear and inelastic deformation mechanisms operate in unirradiated graphite at ambient temperature. Possible inelastic deformation mechanisms in graphite are kink bands [21], twinning [23,24], transformation to the rhombohedral phase [65] and basal dislocation glide [20] (glide of prismatic dislocations in graphite is difficult except at high temperatures [66])

and their potential effect is neglected). Crystal reorientation due to kink bands, twins and phase transformation would introduce additional peaks to the 3DXRD χ_m vs Φ relationship (e.g.,

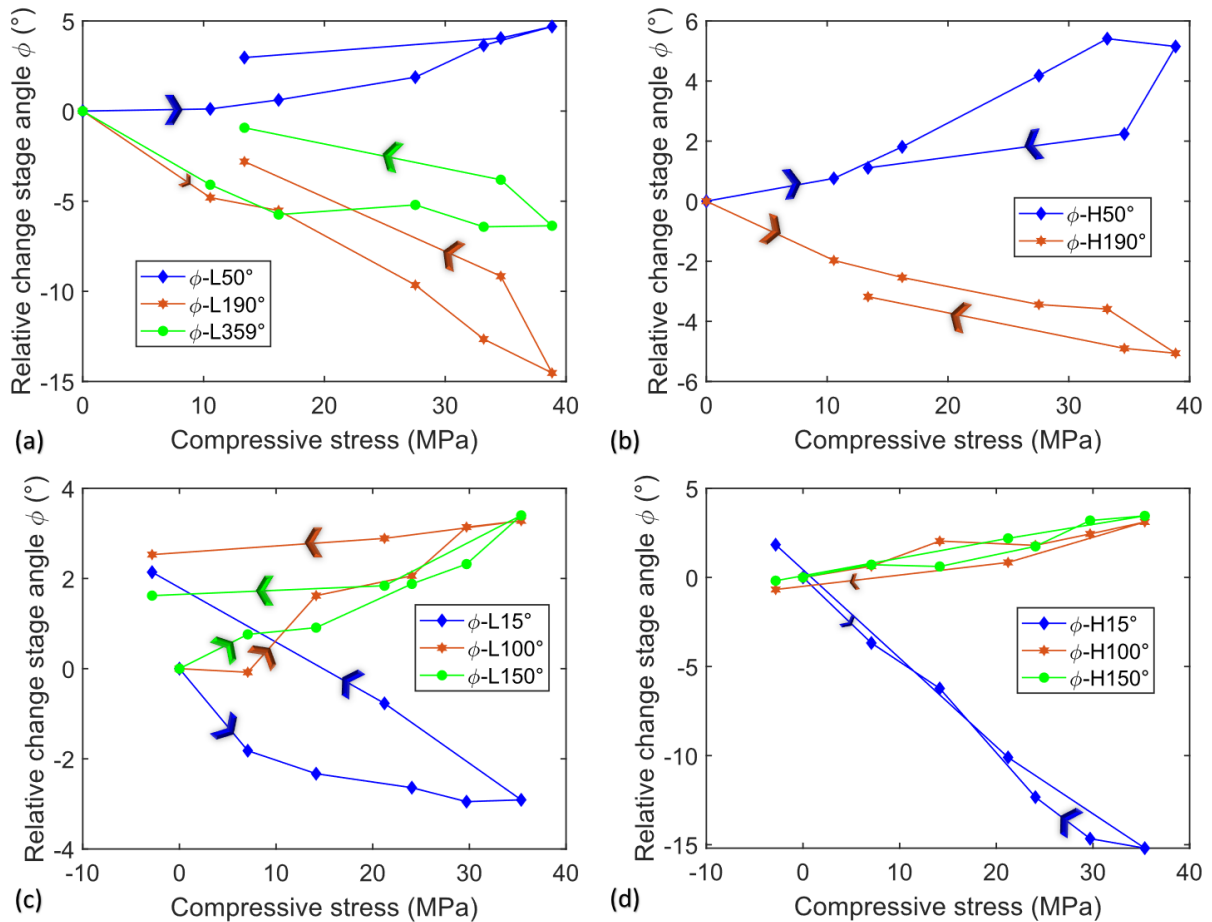


Figure 10). No additional peaks were observed, which suggests that if these crystal reorientation mechanisms did occur, it was not in a significant volume fraction of the gauge volume.

Glide of basal dislocations occurs very readily due to the low shear resistance of the graphite crystal [20,67]. Basal glide would not affect the coherence of the basal planes. Lattice rotation by glide is a common phenomenon in plastic deformation ('Taylor rotation') as grains deform to align the shear direction with the applied strain [68] and in metals it can lead to texture evolution. We propose that the observed lattice reorientations of the crystal domains are predominantly elastic, with a contribution from

shear by basal dislocation glide during loading. On unloading, the shear component to the lattice rotation is not fully recovered. The accommodation of applied strain by such deformations in differently oriented and connected domains of the graphite microstructure would provide the non-linear behaviour that is observed. Incompatible deformations of adjacent domains may lead to high local stresses with strains then accommodated by other inelastic mechanisms including kink bands and twinning, but these are not detectable in the current study.

The shear modulus of the graphite crystal, C_{44} , which varies with the degree of crystallite order [69], is strongly affected by pinning of basal dislocations from crystal defects [67], particularly irradiation-induced point defects [70]. In the event of neutron irradiation, the contribution from basal dislocation glide to shear and rotation of the crystal domains would decrease significantly, with a consequent increase in the effective elastic modulus of the domain towards the intrinsic lattice stiffness. This can explain the observed increase with irradiation of both the linearity of deformation of polycrystalline graphite and its Young's modulus [14]. Future in situ studies to test this hypothesis will study the effects of irradiation and temperature on local changes in strain and crystal orientation, such as via high resolution Bragg-edge neutron tomography [71].

Conclusion

In situ diffraction experiments at different length scales with neutron Bragg-edge imaging and 3DXDRD provide evidence for reorientation of the crystal domains in polycrystalline Gilsocarbon graphite under mechanical stress. The reorientations are predominantly elastic, with a contribution that is not fully recovered on unloading which

is attributed to basal dislocation glide. This observation can explain the effect of fast neutron irradiation on both the linearity of deformation of polycrystalline graphite and its Young's modulus.

Acknowledgments

The authors acknowledge the UK Science and Technology Facilities Council (STFC) for access to neutron beamtime on IMAT at ISIS (Experiment RB1910517), and the European Synchrotron Radiation Facility (ESRF), Grenoble, France for access to X-ray beamline ID11 (Experiment ME1504). We thank Dr Abdalrhaman Mohamed Koko and Dr Yang Chen (University of Oxford), as well as Joachim Paul Forna-Kreutzer (University of Bristol) for their participation in experiment at the ESRF. We are also thankful to Evelina Ametova (Karlsruhe Institute of Technology) for helpful discussion and advice. Thomas Zillhardt is grateful for support from EDF Energy Generation UK.

Author Contributions

Thomas Zillhardt: Methodology, Investigation, Formal analysis, Software, Data Curation, Visualisation, Writing – Original Draft

Genoveva Burca: Investigation, Writing - Review & Editing

Wolfgang Ludwig: Investigation, Writing - Review & Editing

Dong Liu: Writing - Review & Editing

T. James Marrow: Conceptualization, Writing – Original Draft, Supervision, Funding acquisition

Conflicts of interest

The authors have no affiliation with any company nor have any financial interest in the material presented in this manuscript.

References

- [1] M. V Bystrov, I.M. Yachikov, I. V Portnova, Modelling of the thermal state and the melting loss of a graphite electrode in the conditions of the evaporative cooling in the arc furnace, IOP Conf Ser Mater Sci Eng. 966 (2020) 12019. <https://doi.org/10.1088/1757-899x/966/1/012019>.
- [2] K.A. Kuptsov, A.N. Sheveyko, D.A. Sidorenko, D. V Shtansky, Electro-spark deposition in vacuum using graphite electrode at different electrode polarities: Peculiarities of microstructure, electrochemical and tribological properties, Appl Surf Sci. 566 (2021) 150722. <https://doi.org/https://doi.org/10.1016/j.apsusc.2021.150722>.
- [3] D. Sauerteig, S. Ivanov, H. Reinshagen, A. Bund, Reversible and irreversible dilation of lithium-ion battery electrodes investigated by in-situ dilatometry, J Power Sources. 342 (2017) 939–946. <https://doi.org/https://doi.org/10.1016/j.jpowsour.2016.12.121>.
- [4] H. Michael, F. Iacoviello, T.M.M. Heenan, A. Llewellyn, J.S. Weaving, R. Jarvis, D.J.L. Brett, P.R. Shearing, A Dilatometric Study of Graphite Electrodes during Cycling with X-ray Computed Tomography, J Electrochem Soc. 168 (2021) 10507. <https://doi.org/10.1149/1945-7111/abd648>.
- [5] B.J. Marsden, M. Haverty, W. Bodel, G.N. Hall, A.N. Jones, P.M. Mummery, M. Treifi, Dimensional change, irradiation creep and thermal/mechanical property changes in nuclear graphite, International Materials Reviews. 61 (2016) 155–182. <https://doi.org/10.1080/09506608.2015.1136460>.

- [6] B.J. Marsden, A.N. Jones, G.N. Hall, M. Treifi, P.M. Mummery, 14 - Graphite as a core material for Generation IV nuclear reactors, in: P.B.T.-S.M. for G.I.V.N.R. Yvon (Ed.), Woodhead Publishing, 2017: pp. 495–532. <https://doi.org/https://doi.org/10.1016/B978-0-08-100906-2.00014-8>.
- [7] X. Zhou, Y. Tang, Z. Lu, J. Zhang, B. Liu, Nuclear graphite for high temperature gas-cooled reactors, *New Carbon Materials*. 32 (2017) 193–204. [https://doi.org/10.1016/S1872-5805\(17\)60116-1](https://doi.org/10.1016/S1872-5805(17)60116-1).
- [8] X. Zhou, Y. Yang, J. Song, Z. Lu, J. Zhang, B. Liu, Y. Tang, Carbon materials in a high temperature gas-cooled reactor pebble-bed module, *New Carbon Materials*. 33 (2018) 97–108. [https://doi.org/https://doi.org/10.1016/S1872-5805\(18\)60328-2](https://doi.org/https://doi.org/10.1016/S1872-5805(18)60328-2).
- [9] B. Mignacca, G. Locatelli, Economics and finance of Molten Salt Reactors, *Progress in Nuclear Energy*. 129 (2020) 103503. <https://doi.org/https://doi.org/10.1016/j.pnucene.2020.103503>.
- [10] A. Miyahara, T. Tanabe, Graphite as plasma facing material, *Journal of Nuclear Materials*. 155–157 (1988) 49–57. [https://doi.org/https://doi.org/10.1016/0022-3115\(88\)90226-7](https://doi.org/https://doi.org/10.1016/0022-3115(88)90226-7).
- [11] L. Vergari, R.O. Scarlat, Thermodynamics of hydrogen in graphite at high temperature and the effects of oxidation, irradiation and isotopics, *Journal of Nuclear Materials*. 552 (2021) 152797. <https://doi.org/https://doi.org/10.1016/j.jnucmat.2021.152797>.

- [12] S. Yoda, M. Eto, T. Oku, Change in dynamic young's modulus of nuclear-grade isotropic graphite during tensile and compressive stressing, *Journal of Nuclear Materials*. 119 (1983) 278–283. [https://doi.org/10.1016/0022-3115\(83\)90204-0](https://doi.org/10.1016/0022-3115(83)90204-0).
- [13] S. Mrozowski, Mechanical strength, thermal expansion and structure of cokes and carbons, in: A.C. Society (Ed.), *First Biennial Conference on Carbon*, Buffalo, 1953.
- [14] J.E. Brocklehurst, B.T. Kelly, Analysis of the dimensional changes and structural changes in polycrystalline graphite under fast neutron irradiation, *Carbon N Y*. 31 (1993) 155–178. [https://doi.org/10.1016/0008-6223\(93\)90169-B](https://doi.org/10.1016/0008-6223(93)90169-B).
- [15] X. Jin, J. Wade-Zhu, Y. Chen, P.M. Mummery, X. Fan, T.J. Marrow, Assessment of the fracture toughness of neutron-irradiated nuclear graphite by 3D analysis of the crack displacement field, *Carbon N Y*. 171 (2021) 882–893. <https://doi.org/10.1016/J.CARBON.2020.09.072>.
- [16] S.M. Lee, D.S. Kang, J.S. Roh, Bulk graphite: materials and manufacturing process, *Carbon Letters*. 16 (2015) 135–146. <https://doi.org/10.5714/CL.2015.16.3.135>.
- [17] Y. Vertyagina, T.J. Marrow, A multi-scale three-dimensional Cellular Automata fracture model of radiolytically oxidised nuclear graphite, *Carbon N Y*. 121 (2017) 574–590. <https://doi.org/https://doi.org/10.1016/j.carbon.2017.06.031>.
- [18] G. Hall, B.J. Marsden, S.L. Fok, The microstructural modelling of nuclear grade graphite, *Journal of Nuclear Materials*. 353 (2006) 12–18. <https://doi.org/https://doi.org/10.1016/j.jnucmat.2006.02.082>.

- [19] T. Abram, S. Ion, Generation-IV nuclear power: A review of the state of the science, *Energy Policy*. 36 (2008) 4323–4330. <https://doi.org/https://doi.org/10.1016/j.enpol.2008.09.059>.
- [20] D.E. Soule, C.W. Nezbeda, Direct Basal-Plane Shear in Single-Crystal Graphite, *J Appl Phys*. 39 (1968) 5122–5139. <https://doi.org/10.1063/1.1655933>.
- [21] M.W. Barsoum, A. Murugaiah, S.R. Kalidindi, T. Zhen, Y. Gogotsi, Kink bands, nonlinear elasticity and nanoindentations in graphite, *Carbon N Y*. 42 (2004) 1435–1445. <https://doi.org/https://doi.org/10.1016/j.carbon.2003.12.090>.
- [22] T.J. Marrow, I. Šulak, B.S. Li, M. Vukšić, M. Williamson, D.E.J. Armstrong, High temperature spherical nano-indentation of graphite crystals, *Carbon N Y*. 191 (2022) 236–242. <https://doi.org/10.1016/j.carbon.2022.01.067>.
- [23] C. Palache, Contributions to the mineralogy of sterling hill, new jersey: morphology of graphite, arsenopyrite, pyrite, and arsenic, *American Mineralogist*. 26 (1941) 709–717.
- [24] E.J. Freise, A. Kelly, Twinning in Graphite, *Proc R Soc Lond A Math Phys Sci*. 264 (1961) 269–276. <http://www.jstor.org/stable/2414049>.
- [25] A.J. Kennedy, Dislocations and Twinning in Graphite, *Proceedings of the Physical Society*. 75 (1960) 607–611. <https://doi.org/10.1088/0370-1328/75/4/314>.
- [26] J. Skinner, N. Gane, The deformation and twinning of graphite crystals under a point load, *The Philosophical Magazine: A Journal of Theoretical Experimental*

- and Applied Physics. 28 (1973) 827–837.
<https://doi.org/10.1080/14786437308220986>.
- [27] P.J. Heard, M.R. Wootton, R. Moskvic, P.E.J. Flewitt, Deformation and fracture of irradiated polygranular pile grade A reactor core graphite, *Journal of Nuclear Materials*. 418 (2011) 223–232.
<https://doi.org/https://doi.org/10.1016/j.jnucmat.2011.07.003>.
- [28] R. Krishna, A.N. Jones, R. Edge, B.J. Marsden, Residual stress measurements in polycrystalline graphite with micro-Raman spectroscopy, *Radiation Physics and Chemistry*. 111 (2015) 14–23.
<https://doi.org/10.1016/J.RADPHYSICHEM.2015.02.007>.
- [29] T.J. Marrow, D. Liu, S.M. Barhli, L. Saucedo Mora, Y. Vertyagina, D.M. Collins, C. Reinhard, S. Kabra, P.E.J. Flewitt, D.J. Smith, In situ measurement of the strains within a mechanically loaded polygranular graphite, *Carbon N Y*. 96 (2016) 285–302. <https://doi.org/10.1016/j.carbon.2015.09.058>.
- [30] M. Haverty, The microstructure, texture and thermal expansion of nuclear graphite, [Thesis]. Manchester, UK: The University of Manchester; 2015. (2015).
- [31] D. Gonzalez, A. King, M. Mostafavi, P. Reischig, S. Rolland du Roscoat, W. Ludwig, J. Quinta da Fonseca, P.J. Withers, T.J. Marrow, Three-dimensional observation and image-based modelling of thermal strains in polycrystalline alumina, *Acta Mater*. 61 (2013) 7521–7533.
<https://doi.org/10.1016/J.ACTAMAT.2013.06.005>.

- [32] A. King, G. Johnson, D. Engelberg, W. Ludwig, J. Marrow, Observations of Intergranular Stress Corrosion Cracking in a Grain-Mapped Polycrystal, *Science* (1979). 321 (2008) 382 LP – 385.
- [33] T. Zillhardt, A. Koko, Y. Chen, J.P. Forna Kreuzer, W. Ludwig, T.J. Marrow, ME1504: In-situ Mapping of Twinning in Graphite by Diffraction Contrast Tomography @ID11, European Synchrotron Radiation Facility (ESRF). (2018). <https://doi.org/10.15151/ESRF-ES-158876748>.
- [34] L. Renversade, R. Quey, Analysis of in-grain orientation distributions in deformed aluminium using X-ray diffraction and finite elements, in: *IOP Conf Ser Mater Sci Eng*, IOP Publishing Ltd, 2019: p. 012022. <https://doi.org/10.1088/1757-899X/580/1/012022>.
- [35] Y. Hayashi, Y. Hirose, Y. Seno, Polycrystal orientation mapping using scanning three-dimensional X-ray diffraction microscopy, *J Appl Crystallogr.* 48 (2015) 1094–1101. <https://doi.org/10.1107/S1600576715009899>.
- [36] B. März, K. Jolley, T.J. Marrow, Z. Zhou, M. Heggie, R. Smith, H. Wu, Mesoscopic structure features in synthetic graphite, *Mater Des.* 142 (2018) 268–278. <https://doi.org/https://doi.org/10.1016/j.matdes.2018.01.038>.
- [37] G. Song, J. Lin, J. Bilheux, Q. Xie, L. Santodonato, J. Molaison, H. Skorpenske, A. M. Dos Santos, C. Tulk, K. An, A. Stoica, M. Kirka, R. Dehoff, A. Tremsin, J. Bunn, L. Sochalski-Kolbus, H. Bilheux, Characterization of Crystallographic Structures Using Bragg-Edge Neutron Imaging at the Spallation Neutron Source, *J Imaging.* 3 (2017) 65. <https://doi.org/10.3390/jimaging3040065>.

- [38] T.A.C. Zillhardt, G. Burca, D. Liu, T.J. Marrow, In Situ Mechanical Loading and Neutron Bragg-edge Imaging, Applied to Polygranular Graphite On IMAT@ISIS, *Exp Mech.* (2021). <https://doi.org/10.1007/s11340-021-00754-1>.
- [39] E. Fermi, W.J. Sturm, R.G. Sachs, The Transmission of Slow Neutrons through Microcrystalline Materials, *Phys. Rev.* 71 (1947) 589–594. <https://doi.org/10.1103/PhysRev.71.589>.
- [40] A. Reid, I. Martinez, M. Marshall, T. Minniti, S. Kabra, W. Kockelmann, T. Connolley, M. Mostafavi, Mapping of axial plastic zone for roller bearing overloads using neutron transmission imaging, *Mater Des.* 156 (2018) 103–112. <https://doi.org/https://doi.org/10.1016/j.matdes.2018.06.042>.
- [41] Y. Nakai, D. Shiozawa, S. Kikuchi, Y. Nakagawa, K. Asayama, Observations of twinning and detwinning in magnesium alloy by synchrotron radiation DCT and EBSD, in: *Procedia Structural Integrity*, Elsevier B.V., 2019: pp. 83–88. <https://doi.org/10.1016/j.prostr.2020.01.067>.
- [42] H. Proudhon, N. Guéninchault, S. Forest, W. Ludwig, Incipient Bulk Polycrystal Plasticity Observed by Synchrotron In-Situ Topotomography, *Materials.* 11 (2018) 2018. <https://doi.org/10.3390/ma11102018>.
- [43] S.D. Preston, B.J. Marsden, Changes in the coefficient of thermal expansion in stressed Gilsocarbon graphite, *Carbon N Y.* 44 (2006) 1250–1257. <https://doi.org/10.1016/j.carbon.2005.10.045>.
- [44] T.J. Marrow, T. Zillhardt, G. Burca, RB1910517-2: High Resolution Neutron Bragg Imaging of Gilsocarbon Graphite for the Investigation of Crystal

- Reorientation @IMAT, STFC ISIS Neutron and Muon Source. (2020).
<https://doi.org/10.5286/ISIS.E.RB1910517-2>.
- [45] Ch.F. Markides, S.K. Kourkoulis, The influence of jaw's curvature on the results of the Brazilian disc test, *Journal of Rock Mechanics and Geotechnical Engineering*. 8 (2016) 127–146. <https://doi.org/10.1016/J.JRMGE.2015.09.008>.
- [46] C. Keles, L. Tutluoglu, Investigation of proper specimen geometry for mode I fracture toughness testing with flattened Brazilian disc method, *Int J Fract*. 169 (2011) 61–75. <https://doi.org/10.1007/s10704-011-9584-z>.
- [47] R. Chen, F. Dai, J. Qin, F. Lu, Flattened Brazilian Disc Method for Determining the Dynamic Tensile Stress-Strain Curve of Low Strength Brittle Solids, *Exp Mech*. 53 (2013) 1153–1159. <https://doi.org/10.1007/s11340-013-9733-6>.
- [48] A.S. Tremsin, J. V. Vallergera, Unique capabilities and applications of Microchannel Plate (MCP) detectors with Medipix/Timepix readout, *Radiat Meas*. 130 (2020) 106228. <https://doi.org/10.1016/J.RADMEAS.2019.106228>.
- [49] A. Liptak, G. Burca, J. Kelleher, E. Ovtchinnikov, J. Maresca, A. Horner, Developments towards Bragg edge imaging on the IMAT beamline at the ISIS Pulsed Neutron and Muon Source: BEAn software, *J Phys Commun*. (2019). <https://doi.org/10.1088/2399-6528/ab5575>.
- [50] T. Zillhardt, NEUTRONIX: Program for the detection of grain reorientation with in-situ Bragg imaging., (2021). <https://github.com/olayne/NEUTRONIX>.
- [51] A. Mirone, E. Brun, E. Gouillart, P. Tafforeau, J. Kieffer, The PyHST2 hybrid distributed code for high speed tomographic reconstruction with iterative reconstruction and a priori knowledge capabilities, *Nucl Instrum Methods Phys*

Res B. 324 (2014) 41–48.
<https://doi.org/https://doi.org/10.1016/j.nimb.2013.09.030>.

- [52] Suggested methods for determining tensile strength of rock materials, *International Journal of Rock Mechanics and Mining Sciences & Geomechanics Abstracts*. 15 (1978) 99–103. [https://doi.org/10.1016/0148-9062\(78\)90003-7](https://doi.org/10.1016/0148-9062(78)90003-7).
- [53] ASTM D8289 - 19 Standard Test Method for Tensile Strength Estimate by Disc Compression of Manufactured Graphite, (n.d.). <https://www.astm.org/DATABASE.CART/HISTORICAL/D8289-19.htm> (accessed November 20, 2020).
- [54] G. Hondros, The Evaluation of Poisson's Ratio and Young's Modulus of Materials of a Low Tensile Resistance by the Brazilian Test, *Australian Journal of Applied Science*. (1959).
- [55] N.I. Muskhelishvili, Some Basic Problems of the Mathematical Theory of Elasticity, *Some Basic Problems of the Mathematical Theory of Elasticity*. (1977). <https://doi.org/10.1007/978-94-017-3034-1>.
- [56] C.F. Markides, S.K. Kourkoulis, The stress field in a standardized Brazilian disc: The influence of the loading type acting on the actual contact length, *Rock Mech Rock Eng.* 45 (2012) 145–158. <https://doi.org/10.1007/S00603-011-0201-2/FIGURES/14>.
- [57] C.F. Markides, S.K. Kourkoulis, The influence of jaw's curvature on the results of the Brazilian disc test, *Journal of Rock Mechanics and Geotechnical Engineering*. 8 (2016) 127–146. <https://doi.org/10.1016/J.JRMGE.2015.09.008>.

- [58] A. AC10520925, ASTM D3967-16: Standard test method for splitting tensile strength of intact rock core specimens, ASTM Internat., 2008.
- [59] Q.Z. Wang, W. Li, H.P. Xie, Dynamic split tensile test of Flattened Brazilian Disc of rock with SHPB setup, *Mechanics of Materials*. 41 (2009) 252–260. <https://doi.org/10.1016/J.MECHMAT.2008.10.004>.
- [60] Q.Z.Z. Wang, X.M.M. Jia, S.Q.Q. Kou, Z.X.X. Zhang, P.-A. Lindqvist, The flattened Brazilian disc specimen used for testing elastic modulus, tensile strength and fracture toughness of brittle rocks: analytical and numerical results, *International Journal of Rock Mechanics and Mining Sciences*. 41 (2004) 245–253. [https://doi.org/https://doi.org/10.1016/S1365-1609\(03\)00093-5](https://doi.org/https://doi.org/10.1016/S1365-1609(03)00093-5).
- [61] D. Liu, T. Zillhardt, P. Earp, S. Kabra, T. Connolley, T. James Marrow, In situ measurement of elastic and total strains during ambient and high temperature deformation of a polygranular graphite, *Carbon N Y*. 163 (2020) 308–323. <https://doi.org/10.1016/j.carbon.2020.03.020>.
- [62] J.D. Arregui-Mena, W. Bodel, R.N. Worth, L. Margetts, P.M. Mummery, Spatial variability in the mechanical properties of Gilsocarbon, *Carbon N Y*. 110 (2016) 497–517. <https://doi.org/10.1016/J.CARBON.2016.09.051>.
- [63] K. Kusakabe, A. Wake, A. Nagakubo, K. Murashima, M. Murakami, K. Adachi, H. Ogi, Interplanar stiffness in defect-free monocrystalline graphite, *Phys Rev Mater*. 4 (2020) 043603. <https://doi.org/10.1103/PHYSREVMATERIALS.4.043603/FIGURES/6/MEDIUM>.

- [64] S.M. Barhli, L. Saucedo-Mora, M.S.L. Jordan, A.F. Cinar, C. Reinhard, M. Mostafavi, T.J. Marrow, Synchrotron X-ray characterization of crack strain fields in polygranular graphite, *Carbon N Y.* 124 (2017) 357–371. <https://doi.org/10.1016/J.CARBON.2017.08.075>.
- [65] E.J. Freise, A. Kelly, The deformation of graphite crystals and the production of the rhombohedral form, *Philosophical Magazine.* 8 (1963).
- [66] J.G. McHugh, P. Mouratidis, A. Impellizzeri, K. Jolley, D. Erbahar, C.P. Ewels, Prismatic edge dislocations in graphite, *Carbon N Y.* 188 (2022) 401–419. <https://doi.org/10.1016/J.CARBON.2021.11.072>.
- [67] R.H. Telling, M.I. Heggie, Stacking fault and dislocation glide on the basal plane of graphite, <https://doi.org/10.1080/0950083031000137839>. 83 (2010) 411–421. <https://doi.org/10.1080/0950083031000137839>.
- [68] H. Abdolvand, J.P. Wright, A.J. Wilkinson, On the state of deformation in a polycrystalline material in three-dimension: Elastic strains, lattice rotations, and deformation mechanisms, *Int J Plast.* 106 (2018) 145–163. <https://doi.org/10.1016/J.IJPLAS.2018.03.006>.
- [69] I.B. Mason, R.H. Knibbs, The Young's modulus of carbon and graphite artefacts, *Carbon N Y.* 5 (1967) 493–506. [https://doi.org/10.1016/0008-6223\(67\)90026-7](https://doi.org/10.1016/0008-6223(67)90026-7).
- [70] E.J. Seldin, C.W. Nezbeda, Elastic Constants and Electron-Microscope Observations of Neutron-Irradiated Compression-Annealed Pyrolytic and Single-Crystal Graphite, *J Appl Phys.* 41 (2003) 3389. <https://doi.org/10.1063/1.1659430>.

[71] M. Busi, E. Polatidis, F. Malamud, W. Kockelmann, M. Morgano, A. Kaestner, A. Tremsin, N. Kalentics, R. Logé, C. Leinenbach, T. Shinohara, M. Strobl, Bragg edge tomography characterization of additively manufactured 316L steel, *Phys Rev Mater.* 6 (2022) 053602. <https://doi.org/10.1103/PHYSREVMATERIALS.6.053602/FIGURES/4/MEDIUM>.